EVAPORATIVE COOLING PERFORMANCE OF A BRAZED MICROPOROUS COATING ON AN ALUMINUM SURFACE

by

RYAN M. KING

Presented to the Faculty of the Graduate School of

The University of Texas at Arlington in Partial Fulfillment

Of the Requirements for the Degree of

MASTER OF SCIENCE IN MECHANICAL ENGINEERING

THE UNIVERSITY OF TEXAS AT ARLINGTON

DECEMBER 2011

ACKNOWLEDGEMENTS

First, I would like to thank Dr. Seung Mun You for allowing me to perform my research activities in the Microscale Heat Transfer Lab and for all of the guidance and support that he has provided me. Next, I would also like to thank Dr. Miguel Amaya for the advice and insight he was able to give on many issues. Additionally, I would also like to thank Dr. Ratan Kumar and Dr. Hyejin Moon for serving on my defense committee.

I would also like to thank all of the lab members that I have had the privilege to work with during my time at the University of Texas at Arlington. I could have not gotten to this point without their friendship and wisdom.

Lastly, I would like to thank my friends and family for the love and encouragement that they have given me throughout my life. I am truly blessed.

November 23, 2011

ABSTRACT

EVAPORATIVE COOLING PERFORMANCE OF A BRAZED MICROPOROUS COATING ON AN ALUMINUM SURFACE

Ryan M. King, M.S.

The University of Texas at Arlington, 2011

Supervising Professor: Seung Mun You

The effect of an aluminum microporous coating on evaporative cooling performance was studied using distilled water as the working fluid. The aluminum microporous coating was fabricated by brazing aluminum particles to an aluminum substrate. Microporous coating thicknesses of 175 μm ± 20 μm, 270 μm ± 20 μm, and 900 μm ± 90 μm, and average aluminum particle sizes of 27 μm, 70 μm and 114 μm were used in a parametric study to determine the optimum aluminum microporous coating. A hot water treatment maximized the wickability of the microporous coating. Wickability was measured by vertical dipping of the coating. Both a mass approach and a height approach were employed in a vertical dipping test and the results were compared to Washburn's equation. Evaporative cooling tests were then performed on both the microporous coated samples and a plain aluminum reference surface. The results of the evaporative testing were analyzed by plotting heat flux versus average temperature difference between the surface and water. Heat transfer coefficients were plotted versus heat flux. The microporous coating increased evaporation heat transfer by its capillary pumping ability to deliver a film of fluid to a large area. When the particle size was increased from 27 μm to 70 μm the wickability of the microporous coating was enhanced. This enhancement in the wickability of the microporous coating increased the heat transfer coefficient by up to 600 % when compared

to the plain aluminum reference. However, as the particle size increased from 70 μm to 114 μm no significant further increase in wickability or heat transfer performance was observed. Additionally, as the thickness of the microporous coating was increased, a larger volume of fluid was delivered to the heated surface and the onset of dry-out was delayed to higher heat fluxes. The thickest coating, 900 μm ± 90 μm (70 μm particle size), increased the dry-out heat flux 16 times relative to the plain aluminum reference.

TABLE OF CONTENTS

LIST OF ILLUSTRATIONS

Figure Page

LIST OF TABLES

NOMENCLATURE

b	Thickness of the microporous coating (mm)
D	Diffusion coefficient (mm^2/s)
g	Gravity (m/s^2)
h	Heat transfer coefficient (W/m^2-K)
H	Fluid height (mm)
k	Thermal conductivity (W/m-K)
N	Number of measurements
Nu	Nusselt number
Pr	Prandtl number
q”	Heat flux (kW/m^2)
q	Power (W)
r	Characteristic pore radius (μm)
r_{factor}	Roughness
Ra	Rayleigh number
S_x	Standard deviation of the sample
$S_{\bar{x}}$	Standard deviation of the mean
T	Temperature (°C)
t	Time (sec.)
$t_{v,p}$	t-estimator

ΔT Surface temperature – Ambient temperature (°C)

u Uncertainty

v Degrees of freedom

w Width of the microporous coating (mm)

GREEK SYMBOLS

β Coefficient of volume expansion (1/K)

γ Surface tension (N/m)

δ Characteristic length (m)

ε Porosity

η Dynamic viscosity (N-Pa)

θ Intrinsic contact angle (°)

θ^* Effective contact angle (°)

ν Kinematic viscosity of the fluid (m^2/s)

ρ Density (kg/mm^3)

SUBSCRIPTS

1 Temperature at thermocouple location #1

2 Temperature at thermocouple location #2

3 Temperature at thermocouple location #3

4 Temperature at thermocouple location #4

∞ Ambient temperature

0	Zero-order uncertainty
avg	Average of all four thermocouple locations
c	Instrument uncertainty
d	Design stage uncertainty
f	Film temperature
h	Hydraulic radius (μm)
i	Individual sample measurement
P	Probability
v	Degrees of freedom (N-1)
x	Sample
$\bar{x}$	Mean

CHAPTER 1

INTRODUCTION

Heat transfer by means of evaporation is an effective method of cooling heated surfaces and applies to the industrial applications of desalination systems, falling film evaporator tubes, film- fills in cooling towers, evaporative coolers and heat pipes. Evaporation is a more effective method of cooling than single phase due to the large amount of energy removed due to latent heat. Typically, most untreated metallic surfaces are not highly wetting and thus, not capable of spreading fluid, especially against gravity. The microporous coating used in this testing was developed in the University of Texas at Arlington's Microscale Heat Transfer Lab and uses capillary pumping to supply fluid to an extended surface area. The microporous coating consists of aluminum particles that have been brazed to an aluminum substrate. The increase in surface area covered by fluid results in higher rates of heat and evaporative mass transfer. This coating has been named Al-HTCMC, which stands for Aluminum High Temperature Thermally Conductive Microporous Coating.

1.1 Literature Review

Recently, various studies have modified surfaces to enhance wicking and wetting in order to increase the evaporation heat transfer. Iverson et al. [1] measured the rate of evaporation heat transfer of sintered porous copper wicks of varying porosities and thicknesses vertically dipped into a pool of distilled water with a heated upper region. They reported that for a heat flux of 14.6 W/cm^2, the temperature difference between the thermocouple nearest to the evaporator and the thermocouple nearest to the condenser was less than 10 °C. A plain copper bar with the same dimensions, tested at the same heat flux, was shown to produce a

temperature difference of 60 °C. Kim et al. [2] evaluated the spray cooling performance of plain and microporous coated surfaces on both flat and cylindrical heaters. It was determined for spray cooling with a flow rate of 1.75 ml/min, that the microporous coating enhances the heat transfer coefficient by 400 % when compared to the plain, air cooled surface. Hsieh and Yao [3] discussed the effect of a microstructured surface on spray cooling. They noted four distinct heat transfer regimes, flooding, thin film, partial dry-out and dry-out. During the flooding and dry-out regimes there appeared to be no enhancement between the unstructured and structured surfaces. However, in the thin film and partial dry-out regions the microstructured surface showed noticeable enhancement. Kim and Kang [4] studied the effect on the evaporation heat transfer of a hydrophilic coating (by a plasma treatment) on plain, spiral, and corrugated copper tube geometries. This hydrophilic treatment produced receding contact angles as low as 30°, but the highly wetting properties of the surface were temporary. They concluded that the heat transfer rate per unit surface area was 36-45 % higher than plain untreated tubes due to the spreading and creation of a thin film of liquid on the surface of the tube. Xia et al. [5] studied the effect of circumferential microgrooves on an evaporator tube partially immersed in a pool of fluid. The purpose of the microgrooves was to wick and cover the surface with a thin film of liquid. Hanlon and Ma [6] experimentally tested the evaporation heat transfer of a sintered wick structure, horizontally oriented and heated from underneath. The level of fluid in this experiment was kept flush with the top of the wicking structure. It was concluded that in this application there existed a porosity, wick thickness, and average pore radius that maximized the thin film evaporation of the sintered wick. The smaller average pore radius (0.01 mm) was determined to create a thin film of liquid and maximized the rate of evaporative heat transfer.

1.2 Project Objective

The primary objective of this experimental study is to examine the effects of a microporous coating on evaporative cooling of a uniformly heated surface. This study investigates the effects of particle size, thickness and oxidation on both the wickability and the

evaporation heat transfer performance of the microporous coating. To maximize the effect that oxidation had on the wicking characteristics of the microporous coating, an optimum duration of hot water treatment was investigated. The experimental reference case (plain heated surface) was also modeled numerically to resolve the heat transferred through the test heater assembly. Vertical wicking tests were conducted to characterize the wickability of the microporous coating. After these tests were performed, the microporous coated samples were then subjected to evaporative cooling tests in vertical wicking.

CHAPTER 2

EXPERIMENTAL TEST SET-UP AND PROCEDURES

2.1 Aluminum Microporous Coating Fabrication

2.1.1 Coating Paste and Surface Preparation

The aluminum microporous coating consists of 99.7% pure aluminum powder by weight, provided by Valimet Inc., Stoddard solvent (evaporated during brazing process), and a brazing alloy for aluminum. For the parametric study, aluminum powders with average particle sizes of 27 μm, 70 μm, and 114 μm were used. These average particle sizes were determined by using an optical microscope to measure the diameter of 500 particles of each powder. This study of particle distribution is discussed in a later section. The Stoddard solvent is used as a thinning agent for the mixture of aluminum particles and brazing paste. A ratio of 1.0 g: 1.5 g: 1.1 ml, aluminum particles to brazing paste to Stoddard solvent, was proven to yield good bonding after repeated tests. The amount of Stoddard solvent was increased slightly to create thinner coatings (thickness <200 μm). This slight change in the amount of Stoddard solvent does not affect the end coating because the solvent is evaporated at the beginning of the brazing process. The mixture of aluminum particles, brazing paste and Stoddard solvent is mixed vigorously for fifteen minutes before it is applied to the surface of the substrate. Before the microporous coating mixture is applied to the substrate, the substrate is prepared by sanding with 300-grit sand paper and cleaned with isopropyl alcohol in an ultrasonic bath for fifteen minutes. After the mixture is delivered to the surface, the mixture is shaken to allow it to spread evenly on the surface of the substrate.

2.1.2 Brazing Procedure

The filler metal alloy used to braze the microporous coating was provided by Lucas Milhaupt Inc. It consisted of 78 % zinc, 22 % aluminum carried in a paste which includes a flux and a binder. This particular alloy has a liquidus of 462°C, which is below the liquidus of the aluminum substrate making it an acceptable candidate for this application. The brazing process took place in a Sentro-Tech Corporation Oven that has a maximum temperature of 1200 °C. Nitrogen gas was supplied into the oven during the brazing process to create a reduced oxygen environment. This environment curtails oxidation of the microporous coating and the substrate surface. Oxidation interferes with the flow of the melted brazing alloy. From room temperature, the oven is ramped to 80 °C. This temperature is held for sixty minutes to allow the Stoddard solvent to evaporate from the coating. If the oil is not evaporated, the trapped oil will explode through the coating paste creating a coating that is non-uniform and cratered. After the sixty minute dwell time, the oven temperature is ramped from 80 °C to 520 °C where it is held for an additional two minutes to allow the brazing alloys to melt and flow. The coated substrate then is left inside the nitrogen filled oven to cool in order to prevent oxidation.

The actual temperature of the substrate could be different than the oven's programmed temperature. If the temperature of the substrate is not sufficiently high to support brazing, the paste and the coating will have a powdery consistency and come off of the substrate.

2.1.3 Cleaning Protocol

The bonding strength of the microporous coating is evaluated after the sample is cleaned in a 5 % alkali, 95 % distilled water solution ultrasonic bath for fifteen minutes. The sample is then placed in a distilled water ultra sonic bath for an additional fifteen minutes and is then allowed to air dry. The sample is visually inspected again to insure that there is no gap or separation between the microporous coating and the substrate. If a gap is found, the bonding is considered poor and the coating must be redone before any further testing.

2.1.4 Hot Water Treatment

The reactivity between aluminum and water has been well documented [7,8] and was discovered to have an impact on the wickability of aluminum microporous coating. The coating was stabilized in order to prevent oxidation during the evaporative testing by submerging the microporous coating in a hot water (98 °C) bath for one hour. In Section 3.3 it will be shown that this step effectively stabilized the coating for all further testing.

2.1.5 Finalized Aluminum Microporous Coating

A scanning electron microscope (SEM) image of the microporous coating after the brazing, cleaning and hot water bath is depicted in Figure 2.1 at magnifications of x120 and x800.

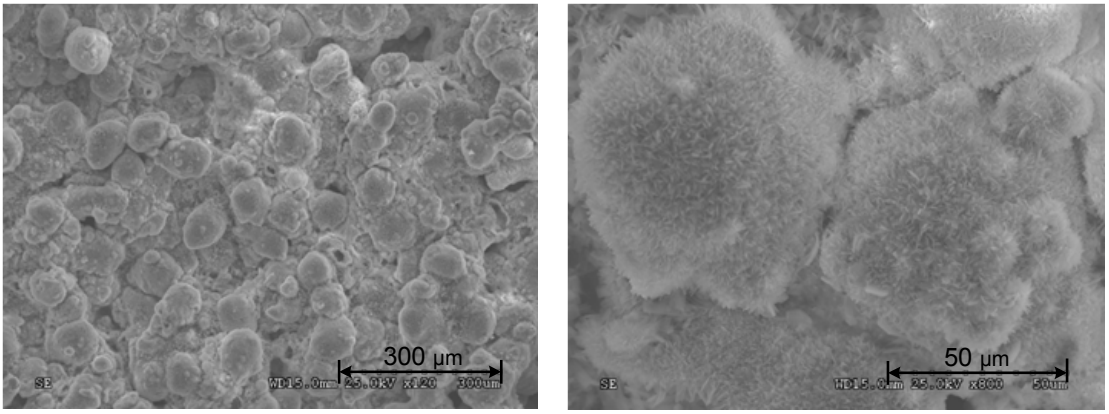

(a) (b)

Figure 2.1 SEM images of the microporous coating at magnifications of (a) x120 and (b) x800.

This particular microporous coating shown in Figure 2.1 is constructed with aluminum powder with an average particle size of 70 µm and its thickness is 250 µm ± 20 µm. From inspection of Figure 2.1 (a), the porous structure created by the interaction of the filler metal and the aluminum powder can be observed. Further magnification of the coating (Figure 2.1 (b)) shows an additional microscale roughness on the surface of the of the microporous coating.

This additional roughness could have an effect on the wicking and wetting characteristics of the microporous coating.

2.2 Evaporative Test Set-up and Procedure

2.2.1 Test Heater

A schematic of the experimental set-up is shown in Figure 2.2 (a). The test heaters used in this experimentation consisted of an aluminum substrate (2.54 cm X 12.7 cm) with a thickness of 2.4 mm, lexan plate, epoxy, rubber heater, and thermocouple wires. Four thermocouple holes were drilled into the edge of the substrate. The first hole was 1.27 cm from one end of the substrate and the subsequent three holes are spaced 2.54 cm apart. The holes have a diameter of 1 mm and a length of 5 mm from the edge of the aluminum substrate. Four T-type (copper/constantan, 30 gage) thermocouples are soldered into the holes with a Kappaloy Inc. 91% Tin, 9 % Zinc solder wire to provide surface temperature measurements. The thermocouple holes were drilled at a depth of 1.2 mm below the aluminum surface and temperature at the surface was calculated assuming one dimensional steady state conduction. A Minco 9535 Silicone Rubber Thermofoil Heater (2.54 cm X 12.7 cm, 38 Ω) was attached to the aluminum substrate using a Duralco 132 High Thermal Conductive Epoxy (k≈ 5.769 W/m-K). While curing the epoxy, the rubber heater was clamped to the aluminum substrate to minimize the thickness of the thermally conductive epoxy layer between the heater and the substrate and to provide uniform bonding. The thermally conductive epoxy was allowed to cure at room temperature for 24 hours. The substrate and the heater were then attached to a lexan plate using 3M Scotch-Weld Epoxy Adhesive DP 420. The heater assembly and the lexan plate were clamped while the epoxy cured for one hour.

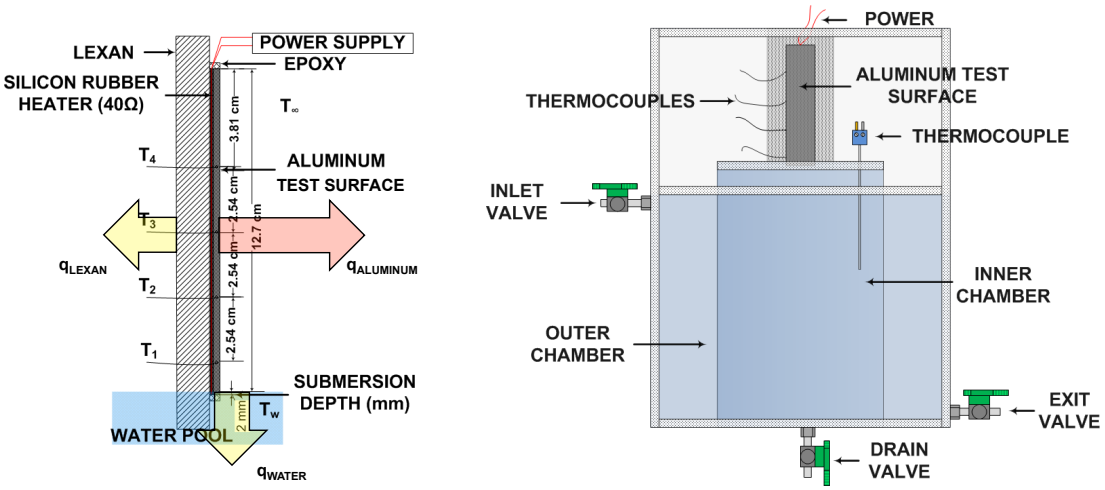

Figure 2.2 Schematic of test heater assembly (a), the test vessel (b) and actual heat transfer paths of the applied heating power (q_{TOTAL}) through the assembly.

2.2.2 Test Vessel and Instrumentation

The power leads from the heater used in the test vessel were connected to an Agilent Technologies N5749A DC Power Supply with an output rating of 7.5 amperes, 100 volts, and 750 watts. The power supply and heater were connected in series with an Agilent Technologies 349854 Multi-function Switch/Measure Unit or DAQ. The current supplied to the heater was determined using an accurate resistor or shunt. The four T-type, copper/constantan, thermocouples are connected to the DAQ and collected by a personal computer. National Instruments Labview software was employed to control the power supply and acquire data. The heater assembly was installed in the test vessel, shown in Figure 2.2 (b). The walls of the test vessel were made of lexan and the dimensions of the test vessel are 38.1 cm (height) X 30.5 cm (width) X 30.5 cm (length). It contained an inner chamber to hold distilled water, the working fluid. The inner chamber was a cylindrical plastic tube with an outer diameter of 11.2 cm, a height of 20.3 cm, and a wall thickness of 0.03 cm. The surrounding space was filled with tap

water and the water was connected to an isothermal bath and circulated. This maintained the distilled water in the inner chamber at a constant 24 °C.

2.2.3 Evaporative Testing Procedure

Before starting the test, the test vessel was cleaned thoroughly with Isopropyl Alcohol. The interior vessel was then filled to a predetermined height with distilled water. The bottom edge of the heater assembly was dipped to a 2 mm depth. In the case of the microporous coated substrates, the fluid wicked through the microporous coating, via capillary pumping. Once the fluid height had reached the top edge of the strip the test was initiated. For the plain aluminum reference, the heater assembly was also dipped to a 2 mm depth. Since no wicking occurred on the surface the test could be started immediately.

A heat flux was applied and the thermocouples were monitored until temperature at thermocouple four, T_4, (see Figure 2.2 (a)) had reached a steady state. From preliminary testing, it was determined that thermocouple four (located 87.9 mm above the distilled water bath) was consistently the final thermocouple to reach the steady-state condition, thus steady state was judged from this thermocouple alone. For each power increment, the approach to steady state was monitored by recording the average of one hundred temperature readings and comparing them to the average of the next one hundred temperature readings. If the difference of the two averages was less than 0.2 °C, the steady state condition was declared and the power was incremented. This process was continued until the system reached a condition of dry-out. The condition of dry-out in this study was not that the entire heated surface had completely dried out, but that thermocouple four had reached a temperature of 120 °C, the temperature limit of the heater. After the test was completed, the total power data was processed in order to account for the heat transfer to the water and to the air through the lexan substrate, labeled as q_{LEXAN} and q_{WATER} in Figure 2.2 (a), and to obtain the correct heat flux to the test surface, $q_{ALUMINUM}$. This correction will be discussed in further detail in Section 2.3.

2.3 Computational Estimations and Corrections

Figure 2.2 depicts the heat transfer paths through the heater assembly. In order to obtain the amount of applied power transferred to the test surface (aluminum substrate), the amount of heat lost to the water, q_{WATER} and to the air through the lexan, q_{LEXAN}, at a given average temperature difference, $\Delta T_{avg}=(T_1+T_2+T_3+T_4)/4-T_{W,}$ between the test surface and water, were found using Ansys Workbench 11.0. The experimental test set-up was modeled in Pro-E Wildfire 3.0 with convective heat transfer boundary conditions as shown in Figure 2.3. A source of internal heat generation was applied to the modeled rubber heater volumes. Appropriate values of convective heat transfer coefficients were found as follows. For the plain aluminum reference case, a condition of single phase heat transfer was assumed. It was understood that the 2 mm submerged part of the aluminum surface would be experiencing negligible two-phase heat transfer. A good agreement with experimental data was obtained using the single-phase assumption. Heat transfer coefficients for the aluminum substrate sections in contact with the air and submerged were estimated using the correlations for natural convection over a vertical plate [9];

$$Ra=\frac{g\beta(T_s-T_\infty)\delta^3}{v^2}Pr \tag{2.1}$$

$$Nu=0.59Ra^{0.25},\ (10^4\leq Ra\leq 10^9) \tag{2.2}$$

$$h=\frac{k}{\delta}Nu \tag{2.3}$$

In order to calculate the Rayleigh number, Ra, a range of surface temperatures, T_s, between 25 °C- 100 °C was assumed. The ambient temperature, T_∞ was taken to be 24 °C, and the properties of the water and air were evaluated at the film temperature, $T_f = (T_s+T_\infty)/2$. The Nusselt number, Nu, is a ratio of the convective heat transfer coefficient, h, to the thermal conductivity, k. From the above equations and assumed temperatures, initial values were

obtained and then adjusted until the calculated ΔT_{avg} matched the experimental ΔT_{avg}. The heat transfer coefficients for natural convection which gave the best match were 8 W/m²K and 2400 W/m²K for the air and the water, respectively. These values fall within the expected range for natural convection.

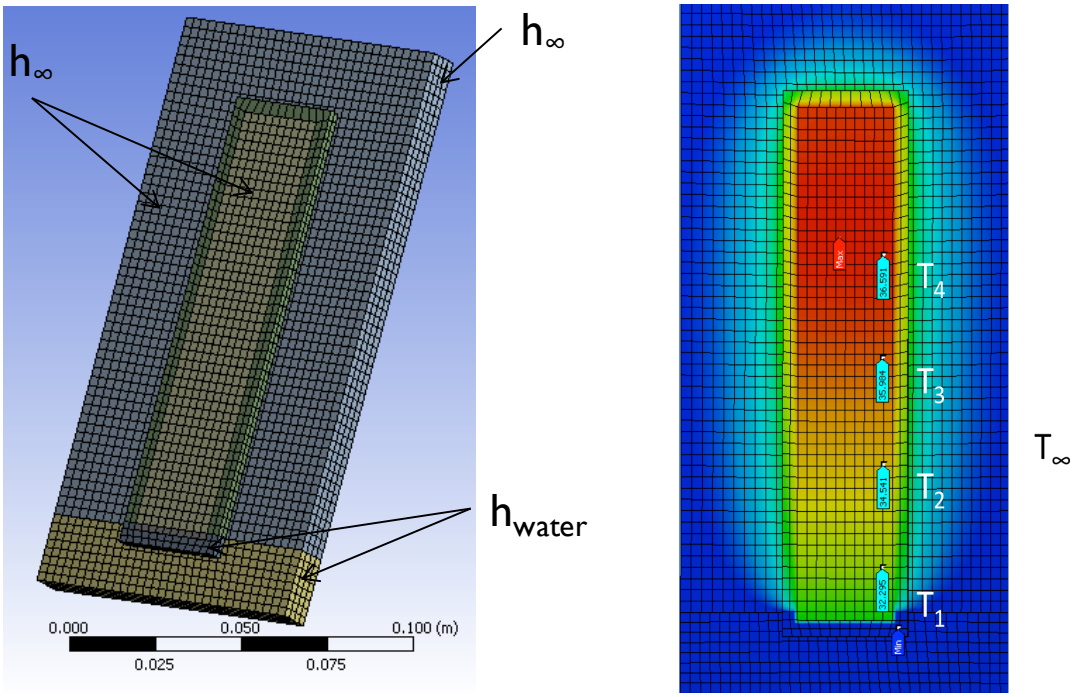

(a) (b)

Figure 2.3 (a) Mesh applied during simulation. (b) Computational temperature contours using an applied internal heat generation of 0.0015 W/cm³.

The simulation was carried out using appropriate values for the internal heat generation power to reproduce the experimental applied powers, q_{TOTAL}. The predicted surface temperature of the computational model was found at the same four locations used in the experiment as Figure 2.3 (b) illustrates. Figure 2.4 compares the average temperature difference versus experimental total applied power between experimental values and computational values for the plain aluminum reference. From the good agreement between the two in Figure 2.4, it was

concluded that the computational model was an accurate representation of the experimental testing.

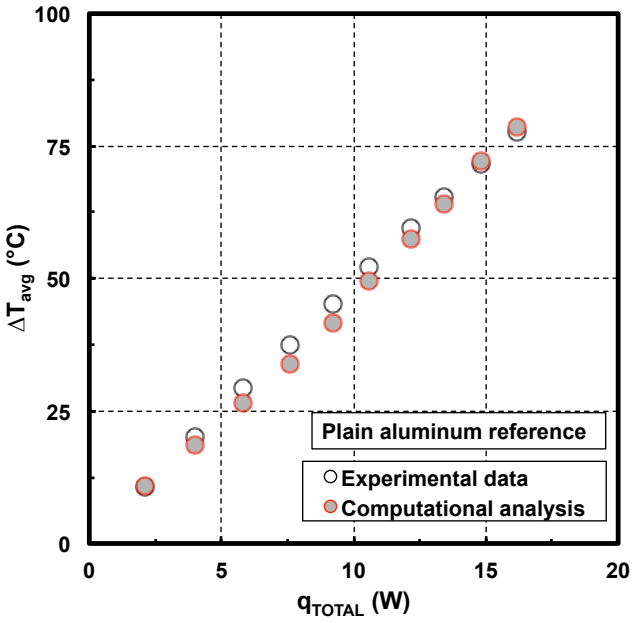

Figure 2.4 Comparison between numerical simulation and experimental data showing average temperature difference between surface and ambient for a given applied power.

From the simulated Ansys Workbench 11.0 model, the amount of heat lost or heat transferred to the distilled water and through the lexan could be calculated for a given ΔT_{avg} and the heat transferred to the surface found by:

$$q_{ALUMINUM}=q_{TOTAL}-q_{WATER}-q_{LEXAN} \tag{2.4}$$

Since the calculated heat losses, q_{WATER} and q_{LEXAN}, are a function only of the ΔT_{avg}, they are valid for the microporous coated surface cases that have the same ΔT_{avg}. Thus, for a known ΔT_{avg}, the amount of the total power transferred to the test surface, $q_{ALUMINUM}$, can be calculated for any total power, q_{TOTAL}. Figure 2.5 shows the linear curve fits of the computational

data for the heat losses as a function of ΔT_{avg}. From this figure, for a given measured ΔT_{avg}, the corresponding amounts of q_{LEXAN} and q_{WATER} were subtracted from the experimental total applied power to yield the actual power, $q_{ALUMINUM}$, to the test surface (eq 2.4).

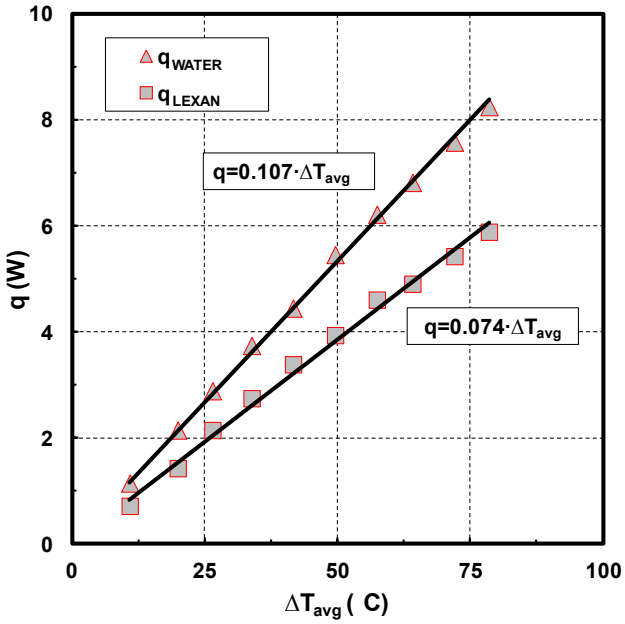

Figure 2.5 Numerically calculated heat loss through the lexan substrate and to the water at a given average temperature difference between surface and ambient.

2.4 Procedure for Measuring the Wickability of the Microporous Coating

2.4.1 Height Approach

The DIN 53924, or the Short Term Longitudinal Wicking Test, is used in industry as the standard for testing the absorption of fluids into textiles and was deemed suitable for testing the microporous coating [10]. The test involves immersing the edge of the microporous coated sample into the fluid. Capillary pumping will cause fluid to absorb into the microporous coating and rise in and along the surface of the strip. Figure 2.6 shows this process in the Al-HTCMC coating.

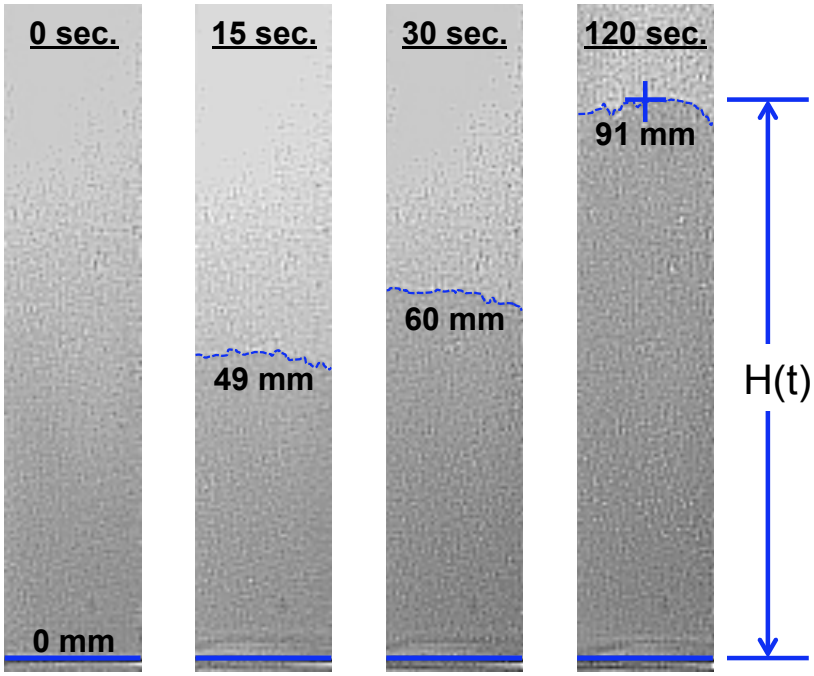

Figure 2.6 Vertical wicking and wetting of pure water into the microporous coating and definition of vertical wicking height

As the figure shows, the wicking height is obvious from the color change of the surface. The rise in the fluid height was recorded using a Vision Research Phantom High Speed Camera v4.3, at a low one hundred frames per second, and analyzed using Phantom Cine Viewer Software. The baseline was set at the location where the aluminum strip came in contact with the distilled water bath and height measurements were taken along a longitudinal axis in the center of the strip. The base line is depicted in Figure 2.6 as a solid blue line. The height measurements were recorded until the fluid had wicked the entire sample or ten minutes had elapsed. Plots of height versus time were used to assess wickability. For instance, the coatings with higher heights for the duration of the experiment were said to more wickable.

2.4.2 Mass Approach

Wickability was also measured by measuring the mass wicked. The mass measurements were taken in a manner similar to that of the height measurements. The

microporous coated sample was dipped into a pool of distilled water and the water was allowed to wick into the microporous coating for a given time period. The coated sample was then weighed using an Acculab VI-1mg Scale and the weight was subtracted from the dry weight of the sample to yield the mass of the liquid that had been wicked into the coating. Height measurements were then derived from the mass approach and compared to the height measurements found by directly measuring the height. This comparison is shown in Section 3.3.

2.5 Particle Size Distribution Study

Aluminum powders provided by Valimet Inc. with sizes of H-30, H-60 and H-95 were used in the fabrication of the microporous coating. The average particle size of each powder was determined using a Nikon SMZ 1500 Optical Microscope and image processing software. For each aluminum powder, the diameter of 500 particles were measured and plotted in the histogram shown in Figure 2.7.

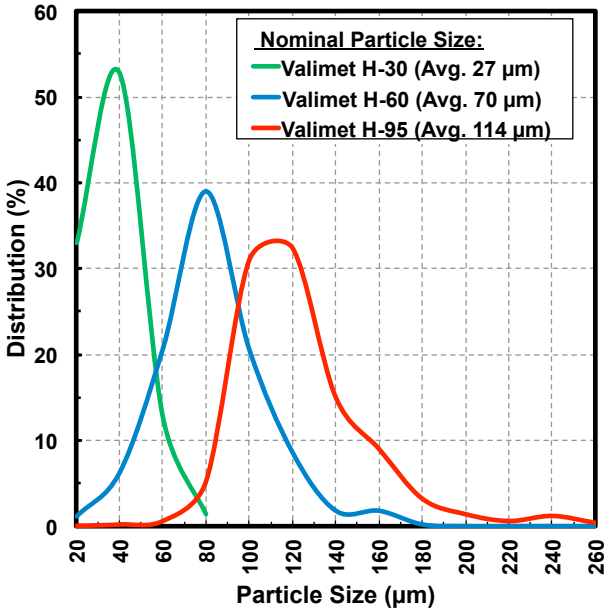

Figure 2.7 Particle size distributions for Valimet aluminum powder rated H-30, H-60 and H-90.

2.6 Uncertainty Analysis

The uncertainty of the temperature measurements was taken to be ± 0.5°C. Uncertainty in the heat flux measurements were found using the the same method as Chang and You [11] and Kim et al. [2] due to the similarities in the test heater and procedure. This uncertainty was estimated to be ± 6% for heat fluxes between 0-50 W/cm². For the height and mass tests, five tests were run on each sample and three samples were created for each change in the coating parameter. The design stage uncertainty, u_d, in the wicking height and mass measurements were determined by the root-mean-squares method [12]. The design stage uncertainty takes into account the instrument uncertainty, u_c, and the zero-order uncertainty, u_0.

$$u_d=\sqrt{u_0^2+u_c^2} \tag{2.5}$$

For the wicking height and mass measurements, the instrument resolution, or the zero-order uncertainty, equals one half the instrument resolution with a probability of 95%. This uncertainty was equal to ± 0.0005 g and ± 0.0005 mm for the mass and height measurements, respectively. The instrument uncertainty was taken to be zero for both height and mass measurements, thus the design stage uncertainty was equal to the zero-order uncertainty. For five repeated tests of one microporous coated surface created with the 70 μm particles and a thickness of 270 μm ± 20 μm, the average height and mass measurements at a time of 30 seconds were found to be 63.8 mm ± 0.6 mm and 0.143 g ± 0.003 g. For the mass measurements, error stemmed from difficulty in repeatability in the test duration. A student t-distribution was applied to determine the confidence interval for the mean value:

$$v=N-1 \tag{2.6}$$

$$S_x=\sqrt{\frac{1}{N-1}\sum_{i=1}^{N}(x_i-\bar{x})^2} \tag{2.7}$$

$$S_{\bar{x}} = \frac{S_x}{\sqrt{N}} \tag{2.8}$$

$$x' = \bar{x} \pm t_{v,P} S_{\bar{x}} \tag{2.9}$$

The number of degrees of freedom associated in data set, v, is equal to one minus the number of measurements, N. The variable, S_x denotes the standard deviation of the sample. The individual sample measurement and the mean sample measurement are denoted by x_i and $\bar{x}$, respectively. The t estimator denoted by $t_{v,P}$ is a function of the probability, P and the degrees of freedom, v. Assuming a 99% probability, the height and mass measurements for the single sample, 70 μm particle size, 270 μm ± 20 μm thick, were found to be 63.8 mm ± 1.2 mm and 0.143 g ± 0.006 g.

CHAPTER 3

RESULTS ON WICKABILITY WITHIN THE MICROPOROUS COATING

3.1 Effect of Hot Water Treatment on Wickability of the Microporous Coating

The impact of oxidation on the wicking and wetting characteristics of hot water treated aluminum substrates is a topic that has been well documented [8]. Due to the chemically active nature of the aluminum surface, an oxide layer will quickly form when the surface is exposed to oxygen or water. Under dry oxygen room temperature conditions, the limiting thickness of the oxide layer is approximately 2.5-3 nm. If the aluminum surface is exposed to water vapor the film thickness is expected to increase [13]. During the exposure to water or vapor the aluminum oxide will hydrate to form a $Al_2O_3(OH)_n$ group, where n is an integer of 1-3. Min and Webb [8] investigated the effects of the wetting and oxidation characteristics of aluminum and copper fin stocks by immersing the fins in either 82 °C or 100 °C water for 20 minutes. They reported that the hot water soak of the aluminum fins increased the wettability of the fins and this increased wettability remained stable for 25 days after the initial hot water soak [8]. This exposure to steam or hot water for a suitable time frame is referred to as the Boehmite treatment. The presence of the hot water or steam accelerates the growth of the oxide layer on the aluminum surface. The microroughing of the aluminum surface due to oxidization improves the surface wetting characteristics [7].

To maximize the effect of oxidation on the wetting characteristics of the microporous coating before all tests, the microporous coating was first subjected to a hot water treatment as indicated in the coating fabrication procedure (Section 2.1.4). A study was performed in order verify the duration of hot water bath which resulted in maximum wetting characteristics. In this study the same microporous coating sample was subjected to a 98 °C hot water treatment for

durations of 20 minutes (blue symbols), 60 minutes cumulative (black symbols), and 120 minutes cumulative (green symbols). In between treatments the wickability was evaluated. .Figure 3.1 depicts the effect of duration of the hot water treatment on the wicking height of the microporous coating. There was a 46% increase in wicking height between the untreated microporous coating and the same microporous coating treated for 60 minutes. Since there appeared to be no significant increase of the microporous coating's wickability with increase in the hot water treatment duration from 60 minutes to 120 minutes, the wickability of the microporous coating was deemed to have stabilized after 60 minutes of treatment. The stabilization was further verified by repeatability of the evaporative test performance, to be discussed in Section 4.1.

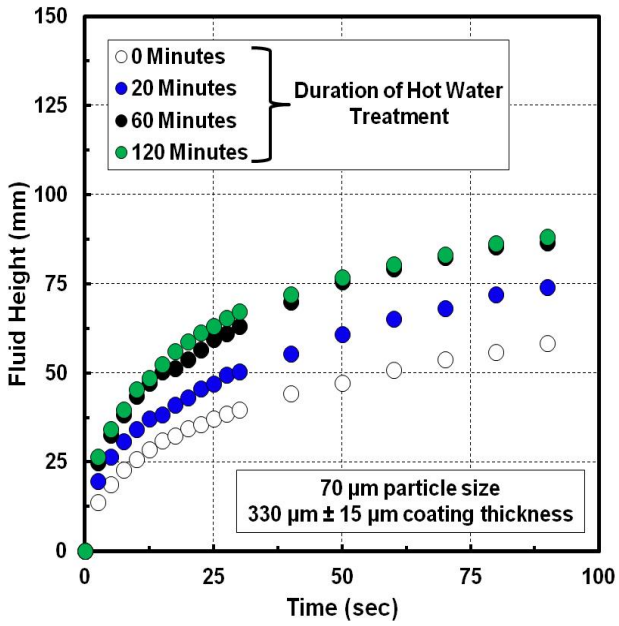

Figure 3.1 Effect of the duration of the hot water treatment on the wicking height of pure water.

From the results of Figure 3.1, there appears to be significant increase in the wicking and wetting characteristics of the microporous coating after hot water treatment. In order to further investigate the effect of the hot water treatment on the microporous coating, scanning

electron microscope (SEM) images were taken before and after the 60 minute hot water treatment. These images are displayed in Figure 3.2. As the magnification increases, it becomes apparent that finer structures are present on the surface of the hot water treated microporous coating. The finer structures could have an influence on the wicking and wetting properties of the microporous coating.

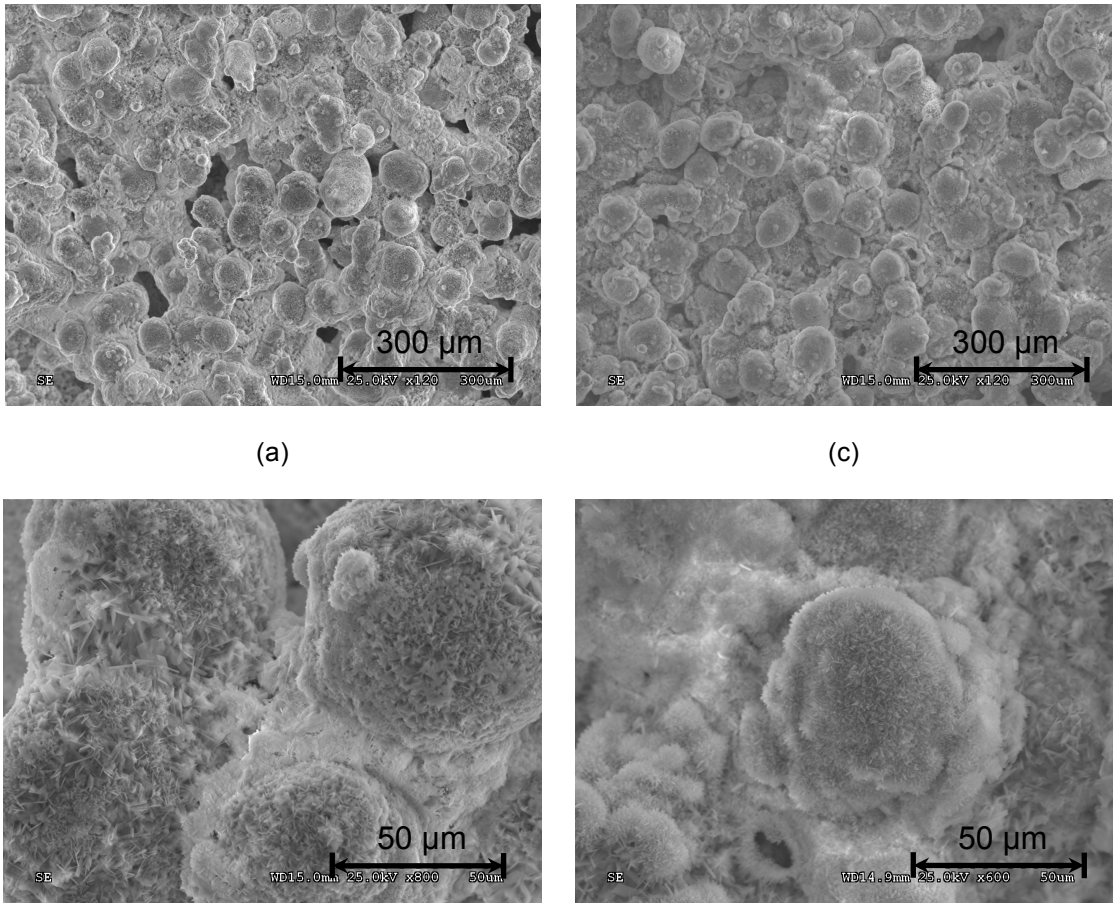

Figure 3.2 SEM images of the untreated microporous coating at magnifications of (a) x120 and (b) x600 and hot water treated microporous coating at magnifications of (c) x120 and (d) x600.

For intrinsic contact angles of less than 90°, the effects of roughening a surface on wettability (through contact angle) are shown by the Wenzel equation [14]:

$$\cos\theta^{*} = r_{factor}\cos\theta \tag{3.1}$$

where θ* is the effective contact angle on the roughened surface, r_{factor} is the roughness factor (ratio of the actual area to the projected area of the roughness), and θ is the intrinsic contact angle. The intrinsic contact angle is the angle that would exist if the surface was perfectly smooth. As the roughnesses increases in eq. 3.1, the effective contact angle on the roughned surface must decrease. For a given volume of fluid, as the contact angle decreases, the area wetted by the fluid must increase. This concept can be applied to both flat surfaces as well as within conduits. Fine structures in the coating could mean an increase in r_{factor} and consequently an increase in the wettability of the pores in the coating.

3.2 Effect of Microporous Coating Particle Size on Wickability

The effect of the particle size on the wickability of the microporous coating was studied using average particle sizes of 27 μm, 70 μm, and 114 μm. The thickness of each microporous coated sample was set as closely as possible to 300 μm to ensure that any enhancement in wickability could be attributed to particle size alone. The experimental results were then compared to the wicking model or theory by the Washburn equation, given by:

$$H^2 = \frac{\gamma\cos(\theta)\, r}{2\eta} t \tag{3.2}$$

where γ is the surface tension, H is the height of the wicked fluid, θ is the intrinsic contact angle, r is the characteristic pore radius, t is time and η is the viscosity [15].

In order for the Washburn equation to be implemented, r and θ must be known or estimated. In order to solve for r, the characteristic pore radius, the wicking test was repeated using a low surface energy fluid, hexane, because hexane has a known contact angle, θ, of zero with most metals. The microporous coatings were dipped into hexane and the fluid height versus time was recorded in the manner identical to the vertical wicking test for distilled water discussed previously. In the Washburn equation (eq. 3.2) the coefficient of t can be simplified by:

$$H^2=Dt \tag{3.3}$$

$$D=\frac{\gamma \cos(\theta)\, r}{2\eta} \tag{3.4}$$

where D is the diffusion coefficient and the slope of the H^2 versus t line. In order to determine the characteristic pore radius of the microporous coating, the diffusion coefficient, D, was determined graphically from the slope of the height squared versus time plot of hexane. These results are shown in Figure 3.3 for the three particle sizes used in this study. The first 0.5 seconds of the vertical wicking tests were selected in order to exclude the effects of gravity and evaporation of the working fluid.

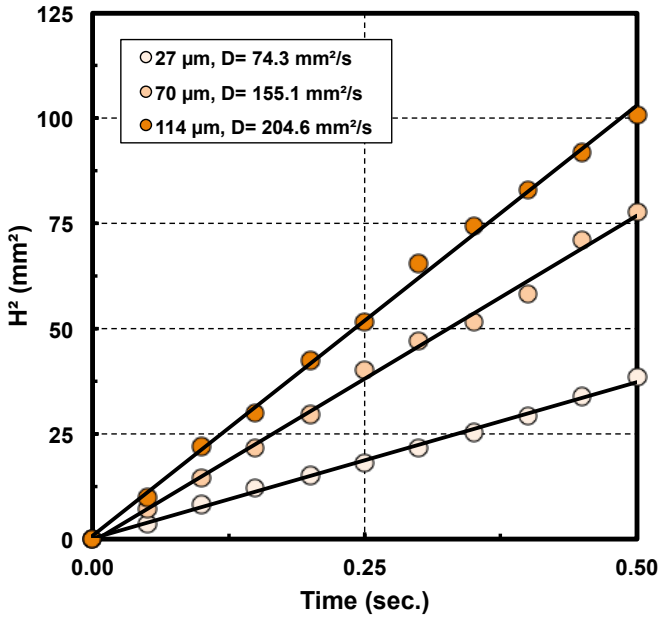

Figure 3.3 Results of vertical wicking test on the microporous coating performed with hexane as the working fluid. The diffusion coefficient, D, is the slope of the curve fitted lines.

After obtaining the slope of the curve fitted lines (Figure 3.3) and substituting a value of zero degrees for the intrinsic contact angle, θ, in eq. 3.4, the r-values (characteristic pore radius) of the microporous coatings could be calculated. Since the r-value is independent of the working fluid, the r-values obtained from the hexane vertical wicking test are valid with distilled

water. Table 3.1 summarizes the r-values and slopes of the curve-fitted lines, D, found for the microporous coatings fabricated with particle sizes of 27 μm, 70 μm, and 114 μm.

Table 3.1 Calculated diffusion coefficient, D, in Figure 3.3, and corresponding calculated characteristic pore radii, r, using hexane as the working fluid.

Average Particle Size (μm)	Diffusion Coefficient (D) (mm^2/s)	Characteristic Pore Radius (r) (μm)
27	74.3	2.4
70	155.1	5.0
114	204.6	6.6

The vertical wicking tests were then performed using distilled water as the working fluid and the diffusion coefficients were found using the method outlined previously for hexane. The effect of particle size on the wickability of distilled water is shown in Figure 3.4. The soild lines are the curve fitted lines from which the diffusion coefficients for water were obtained.

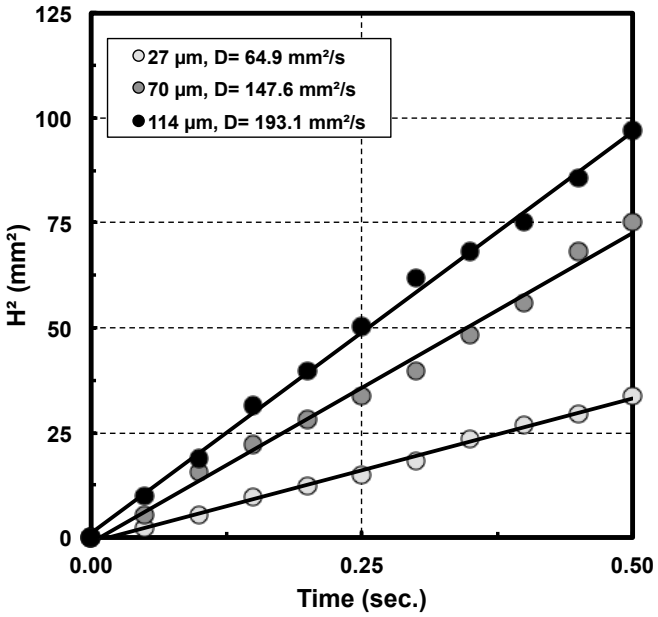

Figure 3.4 Results of vertical wicking test performed with distilled water as the working fluid. Where the diffusion coefficient, D, is the slope of the curve fitted lines.

Once values for the diffusion coefficients were obtained, the intrinsic contact angle for distilled water microporous coating combination could be calculated:

$$\theta = \cos^{-1}\frac{2\eta D}{\gamma r} \tag{3.5}$$

where r is from Table 3.1. Table 3.2 summarizes both the diffusion coefficients of water determined from the wicking tests and the corresponding calculated intrinsic contact angles.

Table 3.2 Calculated diffusion coefficients, D, from Figure 3.4, and corresponding calculated intrinsic contact angle, θ, using distilled water as the working fluid.

Average Particle Size (μm)	**Diffusion Coefficient (mm^2/s)**	**Intrinsic Contact Angle (°)**
27	64.9	47.8
70	147.6	43.0
114	193.1	44.0

Since the intrinsic contact angle is a property of the chemical composition of the material and is not affected by varying particle size, a single average value of 45° ± 2.5° was selected for the intrinsic contact angle. This value was higher than expected for an oxidized aluminum surface [8]. It is believed that the high percentage of zinc used as the filler metal (brazing alloy) prevents the lowering of the contact angle to values seen in oxidized aluminum.

Figure 3.5 presents the fluid rise height for microporous coatings with average particle sizes of 27 μm, 70 μm, and 114 μm for an extended period of time. The time period of 600 seconds, shown in the graph, was selected to attempt to allow enough time for one of the microporous coatings to be wicked to an equilibrium height. The equilibrium height is the wicking height where the capillary forces pulling the fluid are balanced by the weight of the fluid being pulled. From this force balance the equation for equilibrium height can be derived to be:

$$H_e = \frac{2\gamma\cos(\theta)}{r_h \rho g} \tag{3.6}$$

where H_e is equilibrium height, ρ is density, r_h is the hydraulic radius, which is not always equivalent to the capillary or characteristic pore radius, r, and g is gravity [16]. It is believed that the fluid will reach an equilibrium height, but due to limited sample length the equilibrium height was not reached. Therefore equilibrium height and hydraulic radius were not studied.

From the results in Figure 3.5 the microporous coating developed with the smallest average particle size, 27 μm, did not wick or perform as well as the coatings developed with the 70 μm and 114 μm average particle sizes. The coatings made with the 70 μm average particle size (Figure 3.5, black circles), and 114 μm average particle size (dark gray circles) performed comparably to each other. One explanation for the similarity of the wickability of the coatings made with the two larger particle sizes is the tradeoff between capillary pumping and frictional resistance. As the particle size decreases, the passageways, or pore radii, between the particles will also decrease resulting in an increase in the capillary pumping power. However, as the passageways decrease in size, the frictional resistance on the fluid will increase. Another explanation can be found by observation of eq. 3.2, which implies that height, H, is proportional to the square root of the characteristic pore radius, r. As the characteristic pore radius increases, for a given time t, the amount that the fluid height increases will diminish.

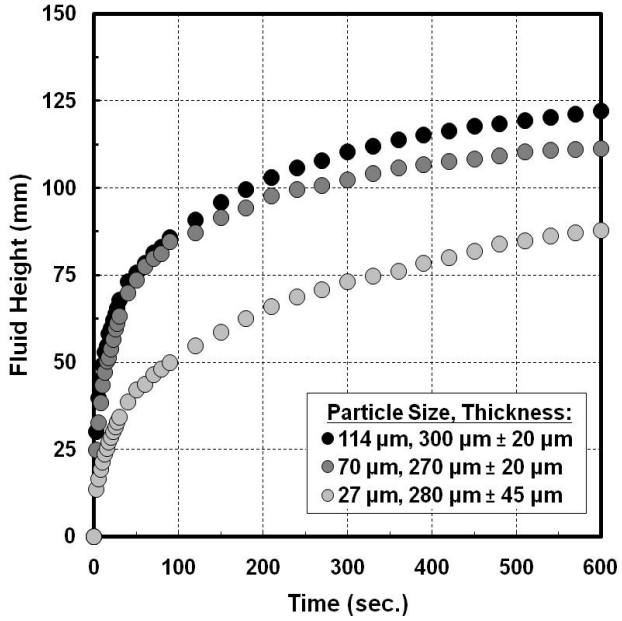

Figure 3.5 Effect of the microporous coating particle size on the wicking height of pure water.

Figure 3.6 depicts a comparison between the results obtained by the Washburn equation and the results found experimentally. In this figure the solid, dashed and dotted lines represent the graph of the Washburn equations using the corresponding r-values and intrinsic contact angle for the 114 µm, 70 µm, and 27 µm average particle sizes (Table 3.1 and Table 3.2), respectively. The black, dark gray and light gray symbols represent the experimental data already shown in Figure 3.5 for the three average particle sizes.

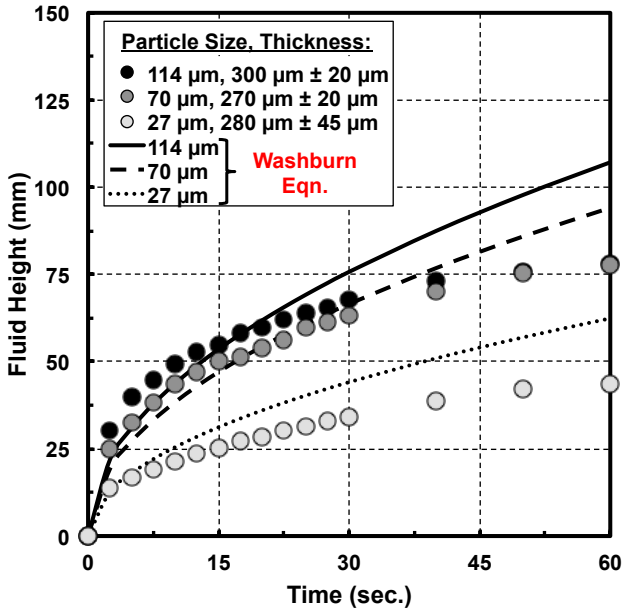

Figure 3.6 Comparison between the wicking height results obtained experimentally and the results obtained from the Washburn equation.

The Washburn equation (eq. 3.2) appears to show similar trends to those obtained experimentally; however, the Washburn equation curves deviate from the experimental data as the duration of the test increases. This deviation could be due partially to evaporation of the test fluid with increasing test duration. Deviation could also be associated with the simplicity of the Washburn equation, which assumes single straight capillary tubes and excludes the effects of gravity.

3.3 Effect of the Microporous Coating Thickness on Wickability

It was important to determine the impact of the microporous coating thickness on the wickability of the coating. It is known from theory that the layers of particles neighboring the substrate will experience high porosity due to the difference in the radius of curvature of the particles and the substrate [17]. Rendall [18] and Graton and Fraser [19] both concluded that higher porosity created by this interaction of the particles and the substrate extended three to

four particle diameters into the packing. Therefore, a thicker coating could be well outside the wall influence zone, while a thinner one might not. Also, filler metals from the brazing process could tend to accumulate towards the wall. Again, a thicker coating could mostly be free from this possible accumulation of brazing alloy near the wall, while a thinner coating might not. The studies by Rendall [18] and Granton and Fraser [19] all involved uniformly sized spheres. Therefore, it is also possible that the non-uniform size of the particles and the presence of a filler metal reduced the effect that the substrate had on the porosity of the microporous coating.

It was understood that by increasing the thickness of the microporous coating the volume capacity of the coating would also increase. In order to remove this known effect from the comparison between samples of different thicknesses, the mass of the fluid wicked into the microporous coating was divided by the coating thickness. A plot of the normalized mass versus time for three microporous coated samples with thicknesses of 175 μm ± 20 μm, 270 μm ± 20 μm, and 900 μm ± 90 μm is shown in Figure 3.7. Due to difficulty in fabrication, microporous coatings with thicknesses less than 175 μm or greater than 900 μm were not created. The average particle size for all three microporous coatings was 70 μm. From the coincidence of curves in Figure 3.7, there was no effect on wickability due to thickness of the microporous coating for coating thicknesses between 175 μm ± 20 μm and 900 μm ± 90 μm. The slight variation in normalized mass wicked by the three coatings in Figure 3.7 was considered to be in the acceptable error range.

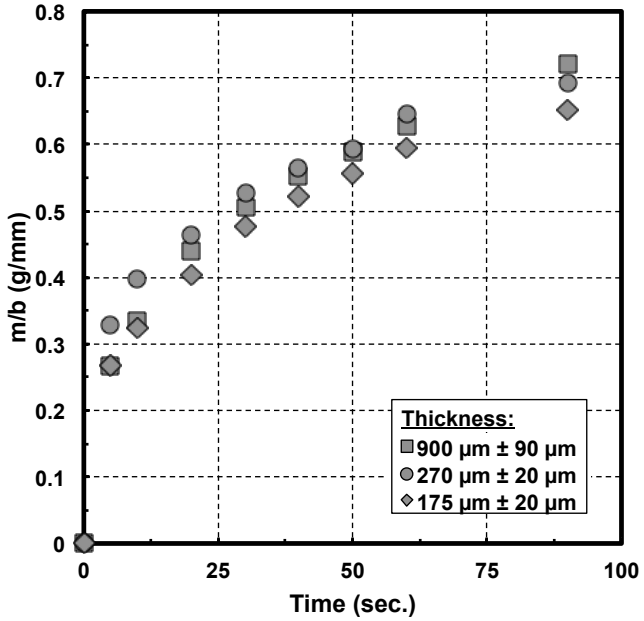

Figure 3.7 Effect of microporous coating thickness on the amount of wicked mass of water (m) per unit thickness (b) of the coating.

This result that thickness does not effect wickability is supported in theory by the Washburn equation, eq 3.2. The Washburn equation excludes the effects of gravity and shows that height is only a function of the characteristic pore radius, fluid properties, and contact angle and not of thickness. The contact angle depends on the type of fluid and surface combination.

The wicked mass measurements of Figure 3.7 were confirmed by comparison to the vertical wicking height measurement data. First, the mass measurements were converted to height by:

$$H = \frac{m}{\varepsilon \rho b w} \tag{3.7}$$

where m is the wicked mass, b and w are the thickness and width of the coating, ε is the porosity, ρ, is the density of water, and H is the wicking height. Porosity was not directly measured, but a reasonable assumption of its value was made. The porosity of a material is

the ratio of the void volume to the total volume; its value is between 0 and 1. The porosities of four modes of spherical, uniform size particle packings were discussed by Haughey and Beveridge [20] and are presented in Table 3.3.

Table 3.3 Four modes of particle packing as listed by Haughey and Beveridge [20].

Type	Process to Obtain Packing	Porosity, ε
Very Loose Random Packing	Fluid velocity is slowly reduced in a fluidized bed.	0.44
Loose Random Packing	Spheres roll into place over similarly place, hand packed.	0.40
Poured Random Packing	Spheres are poured into a container.	0.37 to 0.391
Close Random Packing	Bed is shaken or vibrated vigorously.	0.359 to 0.385

A porosity value of 0.34 yielded heights from eq. 3.7 comparable to those obtained by directly measuring the vertical wicking height. This comparison is displayed in Figure 3.8, which shows height found by derivation from the mass measurements (eq. 3.7, open symbols) and the height found directly from recording height measurements (closed symbols). The porosity is lower than those discussed by Haughey and Beveridge (Table 3.3); however, it is believed to be acceptable since the presence of the filler metal of the brazing process and the un-uniform size of the aluminum particles will lower the porosity [20]. From the results of Figure 3.8, it can be stated that the height measurements and the mass measurements are both valid methods of representing the wickability of the microporous coating and that the thickness of the coating had no effect on wickability.

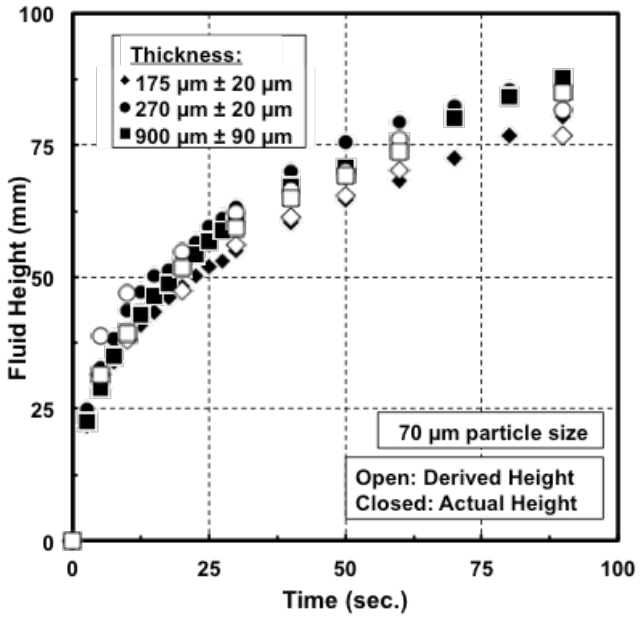

Figure 3.8 Comparison of height measurements taken directly from the height approach to height measurements derived from mass approach.

CHAPTER 4

EFFECT OF THE MICROPOROUS COATING ON EVAPORATIVE COOLING

4.1 Reliability of the Microporous Coating During the Evaporative Test

It was determined from Figure 3.1 that a hot water treatment of 60 minutes appeared to stabilize the wickability of the microporous coating. Figure 4.1 shows the results of evaporative tests on a microporous coating with an average particle size of 70 μm and a coating thickness of 300 μm ± 20 μm that was first hot water treated for 60 minutes. Heat flux, q", on the test surface versus the average temperature difference, ΔT_{avg}, between surface and water are plotted.

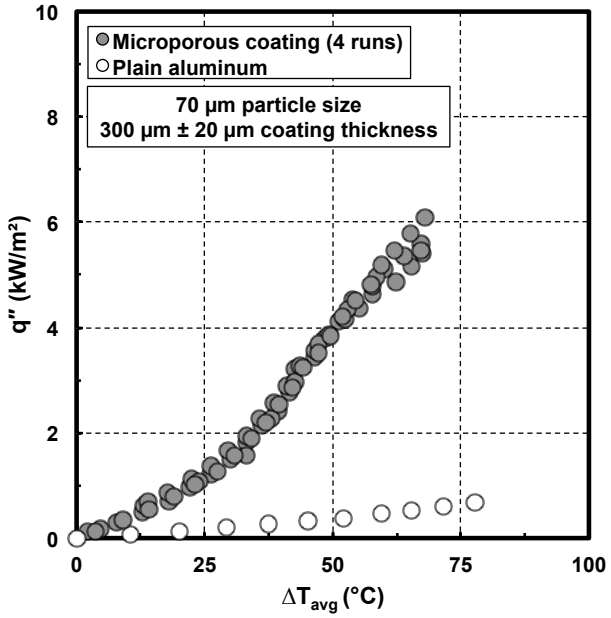

Figure 4.1 Reliability test by 4 repeated runs of the microporous coated heated surface.

Four repeated runs on the same microporous coated surface are shown. The open symbols represent the test on the non-coated aluminum reference curve. For the reference case, an uncoated aluminum substrate with the same dimensions as the samples with the microporous coating was dipped 2 mm into the pool of distilled water. The reference case experiences mostly free convection because there is no microporous coating to wick the fluid. The overlap of the curves for the repeated runs confirms that a 60 minute hot water treatment (98 °C) effectively stabilizes the microporous coating. Therefore in all evaporative testing, the microporous coating was first stabilized with the hot water treatment before any testing as was indicated in the coating fabrication procedure, Section 2.1.4.

4.2 Effect of Microporous Coating Particle Size on Evaporative Cooling Performance

Figure 4.2 shows q" versus ΔT_{avg} for the evaporative cooling tests with microporous coatings with average particle sizes of 27 μm (closed), 70 μm (dark gray) and 114 μm (light gray) and the plain aluminum reference case (open). Figure 4.3 shows the plots of the recession of the of the equilibrium fluid height with heat flux corresponding to the data shown in Figure 4.2. The surface begins to dry-out when the rate of mass transport of the fluid by wicking is less than the rate of mass transport by evaporation of the fluid. During the test the sample was observed to dry out from top to bottom. The equilibrium height to which the fluid had receded down the length of the strip for a given heat flux was recorded and analyzed using the Phantom Cine Viewer Software. Figure 4.3 includes the location of thermocouples on the test surface. For all figures the curves terminate when T_4= 120 °C in order to prevent burning of the heater. When the temperature of thermocouple four, T_4, had reached 120 °C a condition of dry-out was said to have occurred. From Figure 4.3, the strip was not completely dry upon reaching this "dry-out" condition; however, in all cases shown the fluid height had receded to below the height of the thermocouple three, T_3, and cooling was not sufficient to keep T_4 at safe levels. As noted in the Section 2.2.3, the fluid was allowed to wick to reach the top edge of the strip before the test was initiated. Then, with each heat flux increment the height of the fluid in the

microporous coating decreased to an equilibrium height down the length of the microporous coating. Enhancement in evaporation heat transfer is determined by the decrease in the wall superheat at a given heat flux as compared to the plain surface. Since these results involve an average surface temperature and water, they are influenced by the temperatures from the thermocouples located in the dry portion of the test surface.

The thickness of the microporous coating was set at ~300 μm during the particle size study; therefore, any enhancement or degradation of heat transfer can be directly attributed to the changes in the wickability and not to volume capacity change of the coating. The changes in wickability were seen in Figure 3.3. Figure 4.2 reveals that the increasing capillary pumping ability (wickability) of fluid by the microporous coating increases the evaporation heat transfer performance for all heat fluxes compared to plain aluminum. As the heat flux is increased to values greater than 1 kW/m^2, a significant difference in the evaporative cooling performance is observed between 27 μm particle size and the other two sizes, 70 μm and 114 μm. This is similar to results of Figure 3.3, where it was found that by increasing the average particle size in the coating from 27 μm to 70 μm, a large increase in wickability was shown, but upon increasing the particle size from 70 μm to 114 μm there was no further enhancement in wickability. From Figure 4.2, the 70 μm and the 114 μm sizes enhanced the dry-out heat flux 9.9 times that of the plain aluminum reference case.

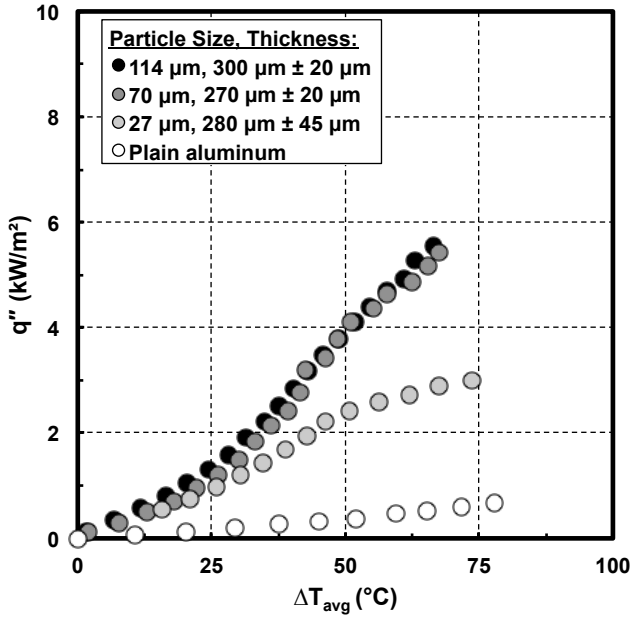

Figure 4.2 Effect of microporous coating particle size on heat transfer performance.

As explained before, Figure 4.3 shows the recession of the equilibrium fluid height with heat flux. As stated earlier, the wickability of the microporous coating increases with the two larger particle sizes (70 µm and 114 µm). This increase in wickability delays the beginning of localized dry-out. As shown in Figure 4.3, for an increasing heat flux, the fluid height is lower, meaning the dry region is larger on the coating made with the smaller particle size (27 µm) as compared to the larger particle sizes (70 µm and 114 µm). For instance at 2 kW/m^2, the wet surface area of the coatings fabricated with the larger particle sizes (70 µm and 114 µm) is approximately ~1.5 times larger than that for the microporous coatings made with the 27 µm size, thus it is expected that the rates of evaporative heat transfer will also be higher for the coatings with larger particle sizes as shown in Figure 4.2

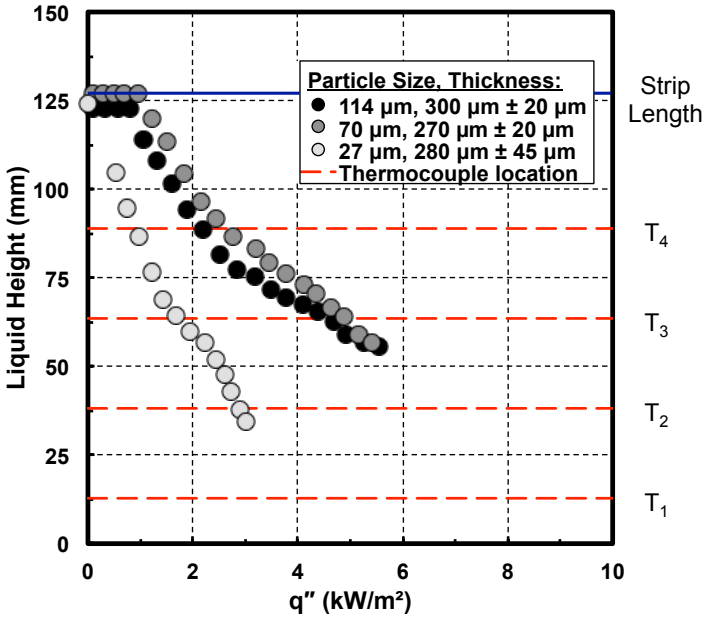

Figure 4.3 Effect of microporous coating particle size on the retreat of equilibrium fluid height with heat flux.

Figure 4.4 shows the effect of the microporous coating particle size on the average heat transfer coefficient versus a heat flux. The presence of the fluid wicked over the surface by the microporous coating, greatly affects the amount of heat transfer compared to the plain reference case. It can be clearly observed that at a given heat flux, the heat transfer coefficient is increased by increasing particle size. The maximum heat transfer coefficient obtained with the 27 µm coating is 6 times that of the plain aluminum case. The maximum heat transfer coefficient is increased 11 times between the 114 µm and the plain aluminum cases. This increase with particle can be attributed to an increase in the liquid available for evaporation due to the better wicking or liquid mass transport of the larger particle sizes (70 µm and 114 µm).

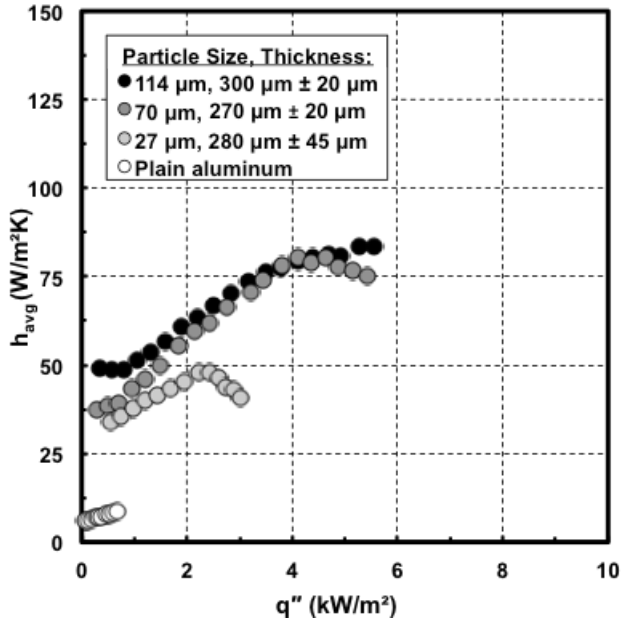

Figure 4.4 Effect of microporous coating particle size on the heat transfer coefficient.

The performance seen in Figure 4.4 can be related to dry-out behavior. From Figure 4.3 partial dry-out begins for the microporous coatings fabricated with the two larger particle sizes (70 µm and 114 µm) at 1 kW/m^2; however, from Figure 4.4, the heat transfer coefficient continues to increase at the same rate until 4 kW/m^2. From this, it is hypothesized that the dry-out region is not completely dry, and that a thin film of liquid exists and is evaporating within the microporous coating causing the continued increase in the heat transfer coefficient. An evaporating thin film can provide enough cooling to continue to increase the heat transfer coefficient because the thin film has a lower thermal resistance. With a lower thermal resistance the surface temperature of the substrate is lower at a given heat flux and ambient temperature. The trend of the increasing heat transfer coefficient changes finally at 4 kW/m^2 because at this point approximately half of the microporous coated strip is visibly dry.

4.3 Effect of Microporous Coating Thickness on Evaporative Cooling Performance

Figure 4.5 shows q" versus ΔT_{avg} for the evaporative cooling tests with the plain aluminum reference curve and the microporous coated samples with thicknesses of 175 μm ± 20 μm (dark gray diamonds), 270 μm ± 20 μm (dark gray circles), and 900 μm ± 90 μm (dark gray squares). An average particle size of 70 μm was used to investigate the thickness effect. Figure 4.6 shows the recession of the fluid height with heat flux. For all heat fluxes, the cooling was significantly improved by the microporous coating relative to the plain surface. For low heat flux values (<1 kW/m^2), the enhancement due to evaporation is equally small for all three thicknesses. However, as the heat flux is increased the effect of coating thickness on rate of evaporation increases. Since the wickability (height versus time behavior) of the microporous coating does not change with thickness (Figure 3.7), the enhancement in heat transfer can be associated with the increase in the volume of the fluid wicked in the coating.

In Figure 4.5, at 3 kW/m^2 and 6 kW/m^2, for the microporous coatings with thicknesses of 270 μm ± 20 μm and 900 μm ± 90 μm, respectively, the slope of both their respective curves decrease signifying slight degradation of evaporative heat transfer. This change in slope corresponds to the recession of the fluid height in the microporous coating to the location of thermocouple four, T_4. Thermocouple four, T_4, is signified in Figure 4.6, as the horizontal dashed red line that intersects the y-axis at 88.5 mm. Since the temperature is an average temperature, it takes into account the temperatures both in the wet and dry portions of the test surface. Once the fluid height recedes below the location of thermocouple four, and this location is no longer cooled by the evaporating fluid, the temperature at thermocouple four, T_4 increases substantially, thus the average temperature increases, which is depicted graphically as the change in the slope at 3 and 6 kW/m^2 in Figure 4.5.

The dry-out heat flux for the thickest coating (900 μm ± 90) μm was delayed to 8 kW/m^2, which results in an enhancement of 14 times compared to the plain aluminum case. The coating thickness of 175 μm ± 20 μm showed an enhancement of 6 times of dry-out heat flux

compared to the plain aluminum case. Thus, the increase of volume of the fluid wicked by the microporous coating both enhanced heat transfer and extended the dry-out heat flux.

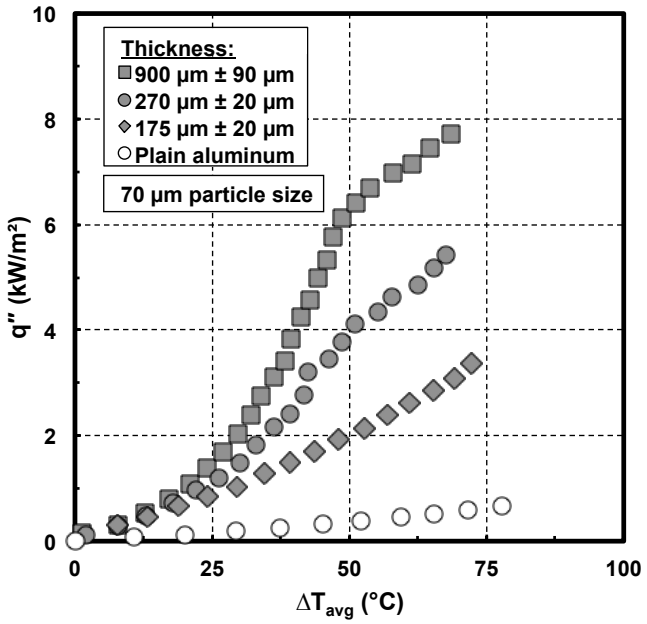

Figure 4.5 Effect of microporous coating thickness on heat transfer performance.

From Figure 4.6, the fluid height immediately begins to recede for the thinnest coating (175 μm ± 20 μm). As the coating thickness increases, the minimum heat flux that starts this localized dry-out also increases. For example, the onset of localized dry-out appears 4 kW/m^2 for the thickest coating (900 μm ± 90 μm). The thicker coating wicks a larger volume of fluid, as discussed in Section 3.1, this increase in the volume of wicked fluid is responsible for heat transfer enhancement. The increase of the wicked volume delays the beginning of localized dry-out.

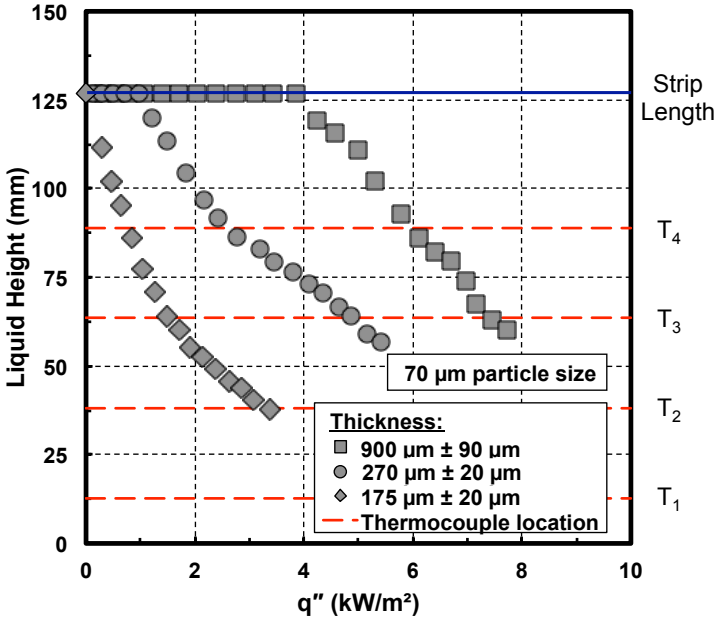

Figure 4.6 Effect of microporous coating thickness on retreat of the equilibrium fluid height with heat flux.

Figure 4.7 compares the average heat transfer coefficient versus heat flux for the three coating thicknesses. The open circles represent the plain aluminum reference case. All microporous coated samples have much greater heat transfer coefficients than the plain aluminum reference case. As the heat flux increases, the difference in the heat transfer coefficient between the coatings of different thicknesses increases. The evaporative cooling provided by the fluid wicked by the microporous coating is responsible for a maximum heat transfer coefficient of 125 W/m^2K at 6 kW/m^2 for the 900 µm ± 90 µm thick coating. This equals an increase of 14 times when compared to the plain aluminum reference case (at q" ≈ 0.8 W/m^2K).

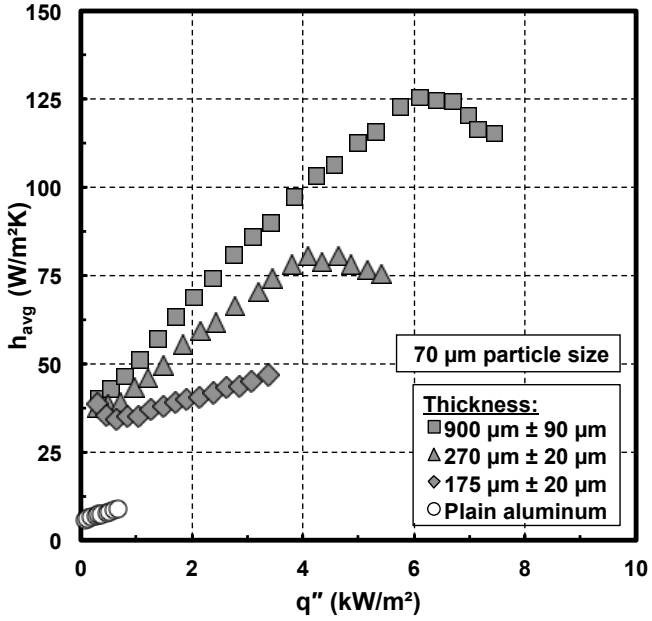

Figure 4.7 Effect of microporous coating thickness on the heat transfer coefficient.

Partial dry-out of the 900 µm ± 90 µm thick coating begins at 4 kW/m^2 (Figure 4.4), however in Figure 4.7 the heat transfer coefficient continues to increase until 6 kW/m^2. As the thickness of the coating increases it is likely that an evaporating thin film a fluid is present inside the coating in the region appearing dry to the naked eye. Once the visibly dry region grows to cover thermocouple four, the average heat transfer coefficient begins to plateau.

CHAPTER 5

CONCLUSIONS AND RECOMENDATIONS

This study investigated the effects of capillary pumping of fluid by the microporous coating on the evaporative heat transfer performance of a vertical test surface. Vertical wicking tests were performed using distilled water as the working fluid to study the effects of coating thickness and particle size on the wickability of the microporous coating. Microporous coating thicknesses of 175 μm ± 20 μm, 270 μm ± 20 μm, and 900 μm ± 90 μm were used in the thickness study, and aluminum particle of average sizes of 27 μm, 70 μm and 114 μm were used in the particle size study. Evaporative cooling tests were then performed on the microporous coated samples and the plain aluminum reference case.

5.1Effect of Hot Water Treatment on Wickability of the Microporous Coating

1. A hot water treatment of 60 minutes on the coating stabilized and maximized the oxidation of the microporous coating. From the repeatability of the thermal test results, the coating did not appear to oxidize further during thermal testing.
2. It is surmised that the hot water treatment enhanced the wettability by the formation of an oxide layer and change in roughness in the microporous coating.

5.2 Effect of Microporous Coating Particle Size on Wickability

1. As the average particle size in the microporous coating was increased from 27 μm to 70 μm there was a significant increase in wickability. At 90 seconds, a 70 % increase in fluid height was noted by increasing the particle size of the coating from 27 μm to 70 μm.
2. As the particle size was increased from 70 μm to 114 μm only a slight enhancement in coating wickability was observed.

3. Using an intrinsic contact angle of 45° ± 2.5°, and characteristic pore radii determined from vertical wicking of hexane into the microporous coating, the Washburn equation supported these trends.

5.3 Effect of Microporous Coating Thickness on Wickability

1. The microporous coating thickness had a minimal effect on the wickability of the microporous coating. This result is consistent with Washburn's model for capillary wicking, which is independent of thickness of the porous medium.
2. Using a porosity estimate of 0.34, a good agreement was found between the wicking height measurements that were measured directly and those that were derived from the wicked mass measurements.

5.4 Effect of Microporous Coating Particle Size on Evaporative Cooling

1. Out of the three average particle sizes tested, the 27 μm particle size coating was the worst performing in both evaporation and wickability tests.
2. The increased wickability of the larger particle size, 70 μm and 114 μm, microporous coatings delayed the beginning of localized dry-out to higher heat fluxes compared to the 27 μm coating.
3. The 27 μm coating was shown to enhance the heat transfer coefficient up to 6 times compared to the aluminum reference. A maximum heat transfer enhancement of 11 times that of the aluminum reference was shown with the 70 μm and 114 μm average particle sizes.
4. The dry-out heat flux was enhanced 10 times by the 70 μm and 114 μm microporous coating compared to the plain aluminum reference.
5. It is possible that a thin film of evaporating water remains within the coating in the visibly dry portion of the coated test surface. This could account for the steady increase in heat transfer coefficient even after the strip has commenced to visibly dry-out.

5.5 Effect of Microporous Coating Thickness on Evaporative Cooling

1. Dry out was further delayed and heat transfer coefficient further increased with increasing thickness of the microporous coating
2. For low heat fluxes (<1 kW/m^2), the evaporation heat transfer coefficient was insensitive to thickness increase.
3. The microporous coating with a thickness of 900 μm ± 90 μm (70 μm particle size) yielded an increase of 12 times in maximum heat transfer coefficient when compared to the plain aluminum reference. The 900 μm ± 90 μm (70 μm particle size) microporous coating increased the dry-out heat flux 16 times relative to the plain aluminum reference.
4. With a thicker coating, it is more likely that a thin evaporating film remains within the visibly dry portion of the coating. This could account for the steady increase in heat transfer coefficient even after the strip has commenced to visibly dry-out.

5.6 Recommendations

1. The 70 μm average particle size provides better bonding when compared to the microporous coating made with the 114 μm particle size.
2. If the fluid were to be dripped or sprayed, it is believed that a thinner coating would perform better due to its ability to spread the drop thinner. Evaporative heat transfer with a new method of applying fluid other than dipping should be investigated. Also, if the fluid is sprayed or dripped a computational correction to obtain the applied heat flux would not be needed.
3. The effect of multi-scale structures on the wickability of a surface should be investigated. Similarly to the effect of microroughening on the surface of the microporous coating, it is believed that by introducing millimeter sized channels or nanoparticles to the microporous coating the wickability could be greatly increased.

4. It is recommended that the brazing procedure be altered in order to insure good bonding. The new brazing procedure should be performed on a high temperature hot plate. The temperature of the hot plate should be set so that the substrate surface temperature is ~570 °C. The filler metal should be allowed ample time to wet and reflow. Once this process concludes the sample can be removed from the hot plate.

APPENDIX A

EXPERIMENTAL DATA

Table A.1 Evaporative test results of the microporous coating with average particle size of 70 μm and thickness of 175 μm ± 20 μm.

Average Particle Size: 70 μm, Thickness: 175 μm ± 20 μm			
ΔT_{avg} [°C]	**q''_{AL}[kW/m²]**	**h_{avg}[W/m²-K]**	**H (mm)**
0.1372	0.0076	55.5327	127
7.6421	0.2952	38.6269	111.754
13.1248	0.4682	35.6696	101.92
18.9598	0.6522	34.3984	95.044
24.1936	0.8498	35.1259	85.914
29.4050	1.0372	35.2730	77.354
34.4523	1.2730	36.9509	70.792
39.2722	1.4817	37.7302	63.944
43.6286	1.7051	39.0830	60.108
48.1470	1.9182	39.8398	55.426
52.7776	2.1371	40.4934	52.719
56.9093	2.3801	41.8232	48.988
61.0157	2.6318	43.1332	45.618
65.2749	2.8423	43.5442	43.776
68.9885	3.0849	44.7157	40.259
72.2152	3.3764	46.7542	37.549

Table A.2 Evaporative test results of the microporous coating with average particle size of 70 μm and thickness of 900 μm ± 90 μm.

Average Particle Size: 70 μm, Thickness: 900 μm ± 90 μm			
ΔT_{avg} [°C]	**q''_{AL}[kW/m²]**	**h_{avg}[W/m²-K]**	**H (mm)**
0.5147	0.0286	55.6212	127.0000
1.4111	0.1395	98.8745	127.0000
7.8710	0.3164	40.1968	127.0000
12.7011	0.5453	42.9371	127.0000
17.1241	0.7981	46.6065	127.0000
20.8640	1.0705	51.3065	127.0000
24.1372	1.3750	56.9679	127.0000
26.9441	1.7062	63.3246	127.0000
29.6766	2.0358	68.5986	127.0000
32.0131	2.3818	74.4002	127.0000
34.0086	2.7458	80.7395	127.0000
36.1392	3.0992	85.7567	127.0000
38.0933	3.4274	89.9740	127.0000
39.5391	3.8403	97.1256	127.0000
41.0365	4.2355	103.2125	119.0640
42.9827	4.5771	106.4868	115.7100
44.3221	4.9959	112.7179	110.7300
45.8396	5.3117	115.8748	101.9700
47.0605	5.7706	122.6217	93.1200
48.6927	6.1165	125.6148	86.0500
51.2601	6.3936	124.7280	82.1320
53.8699	6.6920	124.2253	79.4700
57.9258	6.9661	120.2594	73.9000
61.3433	7.1560	116.6547	67.6200
64.6583	7.4498	115.2177	63.0400
68.5952	7.7142	115.8374	60.1200

Table A.3 Evaporative test results of the plain aluminum reference case.

Plain Aluminum Reference Case			
∆Tavg [°C]	q"AL[kW/m²]	havg[W/m²-K]	H (mm)
0.077931723	0.004303508	55.22152032	
10.61506379	0.062142704	5.854199742	
20.1339363	0.120642447	5.991995047	
29.26154963	0.188717316	6.449327463	
37.53836999	0.261744015	6.972705922	
45.06271754	0.324890155	7.209732856	
51.99728561	0.375589793	7.223257682	
59.47355623	0.460751605	7.747167546	
65.3297456	0.519406784	7.950540429	
71.59835957	0.595018821	8.310509137	
77.79762534	0.674977303	8.676065622	

Table A.4 Evaporative test results of the microporous coating with average particle size of 27 μm and thickness of 280 μm ± 45 μm.

Average Particle Size: 27 μm, Thickness: 280 μm ± 45 μm			
ΔT_{avg} [°C]	**q''_{AL}[kW/m²]**	**h_{avg}[W/m²-K]**	**H (mm)**
0.4702	0.0263	55.9006	124.3900
15.7041	0.5356	34.1046	104.8500
21.0349	0.7492	35.6171	94.6980
25.8814	0.9725	37.5759	86.5320
30.3143	1.2072	39.8214	76.6390
34.6444	1.4330	41.3624	69.0200
38.7784	1.6803	43.3298	64.1460
42.9042	1.9432	45.2923	59.8410
46.4040	2.2197	47.8346	56.6080
50.7096	2.4243	47.8079	52.1050
56.1847	2.6030	46.3289	47.6470
61.9997	2.7244	43.9421	42.6200
67.5330	2.8945	42.8603	37.8850
73.7401	3.0086	40.8006	34.4450

Table A.5 Evaporative test results of the microporous coating with average particle size of 70 μm and thickness of 300 μm ± 20 μm.

Average Particle Size: 70 μm, Thickness: 300 μm ± 20 μm			
ΔT_{avg} [°C]	**q''_{AL}[kW/m²]**	**h_{avg}[W/m²-K]**	**H (mm)**
2.0351	0.1113	54.6863	127.0000
7.7233	0.2877	37.2515	127.0000
12.9119	0.4967	38.4697	127.0000
17.9979	0.7053	39.1856	127.0000
22.1872	0.9643	43.4631	127.0000
26.2058	1.2096	46.1562	119.9550
30.0280	1.4935	49.7384	113.5480
33.0266	1.8309	55.4379	104.3810
36.0874	2.1476	59.5106	96.6650
39.2313	2.4242	61.7931	91.6400
41.6518	2.7667	66.4257	86.4730
42.5096	3.2068	70.4373	83.2110
46.4209	3.4390	74.0831	79.1980
48.4493	3.7919	78.2660	76.4160
51.1445	4.1060	80.2824	73.3150
55.1900	4.3520	78.8553	70.3180
57.6448	4.6389	80.4744	66.6750
62.4174	4.8666	77.9692	63.9860
65.5013	5.1571	76.7334	59.1210
67.5699	5.4192	75.2012	56.7690

Table A.6 Evaporative test results of the microporous coating with average particle size of 114 μm and thickness of 300 μm ± 20 μm.

Average Particle Size: 114 μm, Thickness: 300 μm ± 20 μm			
ΔT_{avg} [°C]	**q''_{AL}[kW/m²]**	**h_{avg}[W/m²-K]**	**H (mm)**
1.4404	0.1119	77.7189	122.7100
6.8573	0.3370	49.1507	122.7500
11.7096	0.5690	48.5903	122.7100
16.3619	0.7957	48.6314	122.7100
20.4112	1.0477	51.3293	113.8200
24.4356	1.3135	53.7533	108.0830
28.1210	1.5933	56.6578	101.7170
31.3382	1.9002	60.6353	94.4240
34.7418	2.2053	63.4782	88.4240
37.6607	2.5112	66.6805	81.5630
40.4457	2.8359	70.1167	77.4130
43.1459	3.1747	73.5798	75.6280
45.7770	3.4885	76.2068	71.5500
48.7508	3.7744	77.4214	69.4090
51.7730	4.0997	79.1854	67.2620
54.5901	4.3832	80.2932	65.6490
57.6223	4.6861	81.3242	62.6620
60.9173	4.9244	80.8380	59.0350
63.0230	5.2636	83.5188	56.5310
66.3717	5.5477	83.5850	55.4760

Table A.7 Run 2 of the evaporative test of the microporous coating with average particle size of 70 μm and thickness of 300 μm ± 20 μm.

Average Particle Size: 70 μm, Thickness: 300 μm ± 20 μm: Run 2		
ΔT_{avg} [°C]	**q''_{AL}[kW/m²]**	**h_{avg}[W/m²-K]**
0.1423	0.0079	55.1313
3.7356	0.1251	33.4833
8.9162	0.3465	38.8607
14.1190	0.5573	39.4685
18.9761	0.7854	41.3879
23.2298	1.0294	44.3144
27.4877	1.2675	46.1104
30.8426	1.5766	51.1165
34.1219	1.9029	55.7691
36.9750	2.2019	59.5519
39.5621	2.5422	64.2578
42.0190	2.8725	68.3609
44.2192	3.2335	73.1233
47.1614	3.5147	74.5253
49.5776	3.8327	77.3076
51.9419	4.2045	80.9457
54.4252	4.5039	82.7540
57.5312	4.8041	83.5038
59.6170	5.1846	86.9653
62.0727	5.4533	87.8542
65.2425	5.7764	88.5374
68.0115	6.0756	89.3325

Table A.8 Run 3 of the evaporative test of the microporous coating with average particle size of 70 μm and thickness of 300 μm ± 20 μm.

Average Particle Size: 70 μm, Thickness: 300 μm ± 20 μm: Run 3		
ΔT_{avg} [°C]	q''_{AL}[kW/m²]	h_{avg}[W/m²-K]
0.2480	0.0137	55.2552
4.7675	0.1760	36.9083
13.9134	0.7018	50.4426
24.0007	1.0675	44.4778
33.0678	1.5773	47.6992
38.0321	2.2624	59.4869
42.6206	2.9653	69.5749
47.1443	3.7009	78.5013
52.8483	4.3374	82.0723
58.5147	4.9607	84.7771
67.2631	5.4494	81.0162

Table A.9 Run 4 of the evaporative test of the microporous coating with average particle size of 70 μm and thickness of 300 μm ± 20 μm.

Average Particle Size: 70 μm, Thickness: 300 μm ± 20 μm: Run 4		
ΔT_{avg} [°C]	**q''_{AL}[kW/m²]**	**h_{avg}[W/m²-K]**
0.2837	0.0158	55.8587
13.0416	0.6226	47.7433
17.7461	0.8601	48.4653
22.2572	1.1105	49.8957
26.1241	1.3757	52.6590
29.6546	1.6683	56.2571
33.0863	1.9460	58.8166
35.7509	2.2750	63.6361
38.6304	2.5613	66.3036
41.1138	2.8959	70.4350
43.6909	3.2580	74.5682
46.4978	3.5692	76.7616
49.3142	3.8547	78.1656
52.3711	4.1679	79.5840
53.8219	4.5337	84.2360
57.7004	4.7973	83.1423
59.9752	5.1096	85.1953
63.7607	5.3520	83.9385
67.2904	5.5912	83.0908

Table A.10 Numerical calculation of heat loss and the comparison between numerical simulation and experimental data.

	Experimental	**Numerical**	**Heat Transfer Paths**		
q_{Total} **[W]**	ΔT_{avg} **[°C]**	ΔT_{avg} **[°C]**	q_{Lexan} **[W]**	q_{Water} **[W]**	$q_{Aluminum}$ **[W]**
2.1000	10.6216	10.8790	0.7200	1.1500	0.2300
4.0000	20.1489	19.9135	1.4300	2.1500	0.4800
5.8000	29.2758	26.4493	2.1500	2.8900	0.6200
7.6000	37.5733	33.8228	2.7500	3.7440	0.8490
9.2000	45.0777	41.6325	3.3900	4.4500	1.1200
10.6000	52.0347	49.5523	3.9400	5.4600	1.2000
12.2000	59.5039	57.4088	4.6100	6.2200	1.3700
13.4000	65.3698	64.0995	4.9100	6.8200	1.6700
14.8000	71.6625	72.0295	5.4300	7.5800	1.7900
16.2000	77.8258	78.5290	5.8900	8.2500	1.9600

Table A.11 Wicking height measurements of the particle size study.

Wickability Tests- Particle Size			
	27 µm	**70 µm**	**114 µm**
Time [sec.]	**Height [mm]**	**Height [mm]**	**Height [mm]**
0	0	0	0
2.5	13.568	24.876	30.061
5	16.631	32.65	39.688
7.5	19.258	38.351	44.979
10	21.446	43.534	49.212
12.5	23.634	47.162	52.919
15	25.385	50.271	54.643
17.5	27.139	51.308	58.208
20	28.452	53.899	59.796
22.5	30.202	56.49	62.189
25	31.515	59.6	64.029
27.5	32.853	61.155	65.617
30	34.141	63.228	67.733
40	38.525	69.965	73.025
50	42.019	75.666	75.671
60	43.767	77.9294	78.318
70	46.395	79.85	81.429
80	48.146	82.482	83.079
90	49.894	84.402	85.725
120	54.711	87.742	90.835
150	58.648	91.302	95.942
180	62.588	94.058	99.467
210	66.088	96.302	102.942
240	68.716	98.923	105.885
270	70.924	101.385	107.823
300	73.092	103.342	110.284
330	74.843	104.372	112.042
360	76.156	105.068	113.875
390	78.343	106.282	115.272
420	80.094	107.852	116.439
450	81.846	108.485	117.684
480	84.034	109.084	118.452
510	84.909	110.102	119.457
540	86.221	110.658	120.182
570	87.097	111.284	121.132
600	87.927	111.852	122.0482

Table A.12 Mass measurements of the coating fabricated with the 27 μm average particle size.

Average Particle Size: 114 μm, Thickness: 302 μm ± 18 μm		
Time [sec]	**Fluid Mass [g]**	**Normalized Mass [g/mm]**
0	0	0.000
5	0.102	0.337
10	0.122	0.403
20	0.149	0.492
30	0.157	0.519
40	0.167	0.552
50	0.184	0.608
60	0.193	0.638
90	0.207	0.684

Table A.13 Mass measurements of the coating fabricated with the 70 μm average particle size.

Average Particle Size: 70 μm, Thickness: 271 μm ± 14 μm		
Time [sec]	**Fluid Mass [g]**	**Normalized Mass [g/mm]**
0	0	0.000
5	0.089	0.328
10	0.108	0.398
20	0.126	0.464
30	0.143	0.527
40	0.153	0.564
50	0.161	0.593
60	0.175	0.645
90	0.188	0.693

Table A.14 Mass measurements of the coating fabricated with the 114 μm average particle size.

Average Particle Size: 27 μm, Thickness: 277 μm ± 45 μm		
Time [sec]	**Fluid Mass [g]**	**Normalized Mass [g/mm]**
0	0	0.000
5	0.036	0.130
10	0.064	0.231
20	0.075	0.270
30	0.083	0.299
40	0.086	0.310
50	0.089	0.321
60	0.092	0.332
90	0.099	0.357

Table A.15 Wicking height measurements of the thickness study.

Wickability Tests: Thickness, Particle Size: 70 µm			
Time [sec]	**176 µm ± 18 µm**	**271 µm ± 14 µm**	**902 µm ± 90 µm**
0	0	0	0
2.5	21.696	24.876	22.47
5	29.104	32.65	28.881
7.5	33.867	38.351	34.856
10	38.1	43.534	39.338
12.5	40.746	47.162	42.823
15	43.392	50.271	46.309
17.5	46.038	51.308	48.798
20	48.154	53.899	51.786
22.5	50.271	56.49	54.2766
25	51.858	59.631	56.766
27.5	52.917	61.155	58.757
30	55.033	63.228	60.749
40	60.325	69.965	67.222
50	64.588	75.666	70.709
60	68.263	77.929	75.687
70	72.469	79.85	80.169
80	76.729	82.482	84.152
90	80.433	84.402	87.638

Table A.16 Mass measurements and the derived height measurements for the 176 μm ± 18 μm microporous coating.

Average Particle Size: 70 μm, Thickness: 176 μm ± 18 μm			
Time [sec]	**Fluid Mass [g]**	**Normalized Mass [g/mm]**	**Height [mm]**
0	0	0.000	0.0000
5	0.047	0.267	31.3885
10	0.057	0.323	38.0669
20	0.071	0.403	47.4166
30	0.084	0.476	56.0985
40	0.092	0.522	61.4412
50	0.098	0.556	65.4483
60	0.105	0.596	70.1232

Table A.17 Mass measurements and the derived height measurements for the 271 μm ± 14 μm microporous coating.

Average Particle Size: 70 μm, Thickness: 271 μm ± 14 μm			
Time [sec]	**Fluid Mass [g]**	**Normalized Mass [g/mm]**	**Height [mm]**
0	0	0.000	0.0000
5	0.089	0.328	38.6656
10	0.108	0.398	46.9200
20	0.126	0.464	54.7400
30	0.143	0.527	62.1256
40	0.153	0.564	66.4701
50	0.161	0.593	69.9456
60	0.175	0.645	76.0278

Table A.18 Mass measurements and the derived height measurements for the 902 μm ± 90 μm microporous coating.

Average Particle Size: 70 μm, Thickness: 902 μm ± 90 μm			
Time [sec]	**Fluid Mass [g]**	**Normalized Mass [g/mm]**	**Height [mm]**
0	0.000	0.000	0.0000
5	0.241	0.267	31.4463
10	0.302	0.335	39.4058
20	0.397	0.440	51.8016
30	0.455	0.504	59.3696
40	0.498	0.552	64.9804
50	0.531	0.588	69.2863
60	0.565	0.626	73.7227

Table A.19 Wicking height measurements with distilled water.

	27 µm-Water	27 µm-Water	70 µm-Water	70 µm-Water	114 µm-Water	114 µm-Water
Time [sec.]	**Height [mm]**	**Height² [mm²]**	**Height [mm]**	**Height² [mm²]**	**Height [mm²]**	**Height² [mm²]**
0.0000	0.0000	0.0000	0.0000	0.0000	0.0000	0.0000
0.0500	1.5110	2.2831	2.3260	5.4103	3.1500	9.9225
0.1000	2.2830	5.2121	3.9370	15.5000	4.3310	18.7576
0.1500	3.1020	9.6224	4.7240	22.3162	5.6060	31.4272
0.2000	3.4890	12.1731	5.3180	28.2811	6.2930	39.6018
0.2500	3.8770	15.0311	5.8120	33.7793	7.0870	50.2256
0.3000	4.2650	18.1902	6.3020	39.7152	7.8740	61.9999
0.3500	4.8570	23.5904	6.9540	48.3581	8.2680	68.3598
0.4000	5.1850	26.8842	7.4800	55.9504	8.6610	75.0129
0.4500	5.4280	29.4632	8.2680	68.3598	9.2550	85.6550
0.5000	5.8150	33.8142	8.6610	75.0129	9.8430	96.8846

Table A.20 Wicking height measurements with hexane

	27 µm-Hexane	27 µm-Hexane	70 µm-Hexane	70 µm-Hexane	114 µm-Hexane	114 µm-Hexane
Time [sec.]	**Height [mm]**	**Height² [mm²]**	**Height [mm]**	**Height² [mm²]**	**Height [mm²]**	**Height² [mm²]**
0	0	0	0	0	0	0
0.05	1.938	3.755844	2.714	7.365796	3.151	9.928801
0.1	2.8854	8.32553316	3.789	14.356521	4.696	22.052416
0.15	3.488	12.166144	4.665	21.762225	5.472	29.942784
0.2	3.875	15.015625	5.452	29.724304	6.523	42.549529
0.25	4.263	18.173169	6.343	40.233649	7.182	51.581124
0.3	4.65	21.6225	6.865	47.128225	8.102	65.642404
0.35	5.038	25.381444	7.188	51.667344	8.632	74.511424
0.4	5.425	29.430625	7.642	58.400164	9.102	82.846404
0.45	5.813	33.790969	8.423	70.946929	9.582	91.814724
0.5	6.2	38.44	8.823	77.845329	10.032	100.641024

Table A.21 Wicking height measurements derived from the Washburn equation.

	27 µm-Water	70 µm-Water	114 µm-Water
Time [sec.]	**Height [mm]**	**Height [mm]**	**Height [mm]**
0.0000	0.0000	0.0000	0.0000
2.5000	12.7391	19.2093	21.8712
5.0000	18.0158	27.1660	30.9306
7.5000	22.0648	33.2715	37.8821
10.0000	25.4782	38.4186	43.7424
12.5000	28.4855	42.9533	48.9055
15.0000	31.2043	47.0529	53.5733
17.5000	33.7045	50.8230	57.8658
20.0000	36.0317	54.3321	61.8611
22.5000	38.2173	57.6278	65.6136
25.0000	40.2846	60.7451	69.1629
27.5000	42.2509	63.7100	72.5386
30.0000	44.1296	66.5429	75.7641
40.0000	50.9565	76.8371	87.4849
50.0000	56.9710	85.9065	97.8110
60.0000	62.4087	94.1059	107.1466
70.0000	67.4090	101.6460	115.7316
80.0000	72.0633	108.6641	123.7223
90.0000	76.4347	115.2557	131.2273
120.0000	88.2592	133.0858	151.5282
150.0000	98.6767	148.7945	169.4137
180.0000	108.0950	162.9962	185.5834

REFERENCES

[1] Iverson, B. D., Davis, T. W., Garimella, S. V., 2007, "Heat and Mass Transport in Heat Pipe Wick Structures," Journal of Thermophysics and Heat Transfer, **21**(2) pp. 392.

[2] Kim, J. H., You, S. M., and Choi, S. U. S., 2004, "Evaporative Spray Cooling of Plain and Microporous Coated Surfaces," International Journal of Heat and Mass Transfer, **47**(14-16) pp. 3307-3315.

[3] Hsieh, C., and Yao, S., 2006, "Evaporative Heat Transfer Characteristics of a Water Spray on Micro-Structured Silicon Surfaces," International Journal of Heat and Mass Transfer, **49**(5-6) pp. 962-974.

[4] Kim, H., and Kang, B. H., 2003, "Effects of Hydrophilic Surface Treatment on Evaporation Heat Transfer at the Outside Wall of Horizontal Tubes," Applied Thermal Engineering, **23**(4) pp. 449-458.

[5] Xia, Z. Z., Yang, G. Z., and Wang, R. Z., 2008, "Experimental Investigation of Capillary-Assisted Evaporation on the Outside Surface of Horizontal Tubes," International Journal of Heat and Mass Transfer, **51**(15-16) pp. 4047-4054.

[6] Hanlon, M. A., and Ma, H. B., 2003, "Evaporation Heat Transfer in Sintered Porous Media," Journal of Heat Transfer, **125**(4) pp. 644-652.

[7] Nikaido, N., Shirai, S., Iihashi, M., 1976, "Process for Treating the Surface of Aluminum of Aluminum Alloy," (3,945,899) .

[8] Min, J., and Webb, R. L., 2002, "Long-Term Wetting and Corrosion Characteristics of Hot Water Treated Aluminum and Copper Fin Stocks," International Journal of Refrigeration, **25**(8) pp. 1054-1061.

[9] Cengel, A., and Turner, R., 2005, "Fundamentals of Thermal-fluid Science," McGraw-Hill, New York, pp. 579-590.

[10] Patnaik, A., Rengasamy, R. S., Kothari, V. K., 2006, "Wetting and Wicking in Fibrous Materials," Textile Progress, **38**(No 1) pp. 40-46.

[11] Chang, J. Y., and You, S. M., 1997, "Enhanced Boiling Heat Transfer from Microporous Surfaces: Effects of a Coating Composition and Method," International Journal of Heat and Mass Transfer, **40**(18) pp. 4449-4460.

[12] Figliola, R.S., and Beasley, D.E., 2006, "Theory and Design for Mechanical Measurements," pp. 110-155.

[13] Hatch, J.E., 1984, "Aluminum: properties and physical metallurgy," American Society for Metals, Ohio, pp. 17.

[14] Wenzel, R. N., 1949, "Surface Roughness and Contact Angle'" J.Phys.Colloid Chem., **53**(9) pp. 1466.

[15] Washburn, E. W., 1921,"Dynamics of Capillary Flow," Phys.Rev., **17**(3) pp. 273.

[16] Hamraoui, A., and Nylander, T., 2002, "Analytical Approach for the Lucas–Washburn Equation," Journal of Colloid and Interface Science, **250**(2) pp. 415-421.

[17] Dullien, F.A.L., 1992, "Porous Media: Fluid Transport and Pore Structure," Academic Press, Inc., New York, .

[18] Rendell, M. J., 1963, J. Ramsey Soc. Chem. Eng., **10** pp. 31.

[19] Granton, L. C., and Frazer, H. J., 1935, J. Geol., **43** pp. 785.

[20] Haughey, D. P., and Beveridge, G. S. G., 1969, "Structural Properties of Packed Beds: A Review." The Canadian Journal of Chemical Engineering, **47**(2) pp. 130-140.

BIOGRAPHICAL INFORMATION

Ryan M. King obtained a Bachelor of Science in Mechanical Engineering from the University of Texas at Arlington in 2008. He then began work on a Master of Science in Mechanical Engineering where he performed his research in the Microscale Heat Transfer Lab under the supervision of Dr. Seung Mun You. His researched focused on enhancing evaporative heat transfer by creating a highly wicking and wetting surface.